Journal of Quantitative Spectroscopy & Radiative Transfer 347 (2025) 109629

Contents lists available at ScienceDirect

Journal of Quantitative Spectroscopy and Radiative Transfer

journal homepage: www.elsevier.com/locate/jqsrt

Survey of the updated Oxygen line list in the HITRAN2024 spectroscopic database☆

Erin M. Adkins [a],[*], Joseph T. Hodges [a], Katarzyna Bielska [b], Alain Campargue [c], Roman Ciuryło [b], Jolanta Domysławska [b], Rafael P. Fernandez [d,e], Hélène Fleurbaey [c], Maciej Gancewski [b], Hubert Jóźwiak [b], Samir Kassi [c], Daniel Lisak [b], Didier Mondelain [c], Gustavo G. Palancar [f,g,h], Wilfrid Somogyi [i], Orlando G. Tomazzeli [d,e], Ha Tran [j], Piotr Wcisło [b], Szymon Wójtewicz [b], Sergei N. Yurchenko [i], Iouli E. Gordon [k],[*]

[a] National Institute of Standards and Technology, Gaithersburg, MD 20899, USA
[b] Institute of Physics, Faculty of Physics, Astronomy and Informatics, Nicolaus Copernicus University in Toruń, Grudziądzka 5, 87-100 Toruń, Poland
[c] Univ. Grenoble Alpes, CNRS, LIPhy, 38000 Grenoble, France
[d] Instituto Interdisciplinario de Ciencias Básicas (ICB-CONICET), Mendoza, Argentina
[e] Facultad de Ciencias Exactas y Naturales, Universidad Nacional de Cuyo (FCEN-UNCuyo), Mendoza, Argentina
[f] INFIQC: Instituto de Investigaciones en Fisicoquímica de Córdoba (CONICET-UNC), Córdoba, Argentina
[g] Departamento de Fisicoquímica, Facultad de Ciencias Químicas, Universidad Nacional de Córdoba, Córdoba, Argentina
[h] Centro Láser de Ciencias Moleculares, Universidad Nacional de Córdoba, Córdoba, Argentina
[i] Department of Physics and Astronomy, University College London, Gower Street, London WC1E 6BT, United Kingdom
[j] Laboratoire de Météorologie Dynamique, IPSL, CNRS, Sorbonne Université, Ėcole normale supérieure, PSL Research University, Ėcole polytechnique, F-75005 Paris, France
[k] Atomic and Molecular Physics Division, Harvard-Smithsonian Center for Astrophysics, Cambridge, MA, USA

ARTICLE INFO

Keywords:
HITRAN database
O_2
Line intensity
Line-shape parameters

ABSTRACT

Light–matter interactions involving molecular oxygen (O_2) span numerous decades in the frequency of electromagnetic radiation and are important to many thermophysical and thermochemical mechanisms, ranging from atmospheric remote sensing of greenhouse gases, aerosols, pollutants, temperature and pressure, visible and infrared radiative exchange in the upper atmosphere, ozone formation and decomposition, and the search for life beyond Earth, among many other examples. Here, we highlight advances in the quantitative spectroscopy of O_2, for which updated band-specific, line-by-line parameters have been provided in the HITRAN2024 spectroscopic database. Theoretical results are presented for electric quadrupole transition intensities in the ground state of $^{16}O_2$, and the Noxon band in the near-infrared region has been included in HITRAN for the first time. Particular focus is placed on the 1.27 μm, A- and B-bands of O_2, in which intensities, line-shape (including beyond-Voigt parameterizations), and position parameters with improved accuracy and/or extended spectral coverage are presented. Corrections to the Schumann–Runge bands are also reported. The paper closes with recommendations and an outlook on key challenges in advancing our understanding of the spectroscopy of O_2.

1. Introduction

Molecular oxygen (O_2) plays an important role in the atmosphere and at the surface of the Earth. It is relevant to a myriad of physical, chemical, and biogeochemical processes, ranging from photolysis of O_2 to form stratospheric ozone which prevents solar ultraviolet radiation from reaching the ground [1], heating in the mesosphere from absorption of solar radiation involving the A-, B- and γ-bands of O_2 plus subsequent exothermic reactions [2], photosynthesis and respiration by living organisms [3], as well as oxidation of fuels for energy production. For remote sensing observations of atmospheric gases from ground- and satellite-based spectrometers, the well-mixed and stable amount fraction (≈20%) of O_2 in the atmosphere can be probed using spectroscopic methods to yield airmass and surface pressure from column-integrated atmospheric retrievals [4–6], cloud height/coverage

---

☆ This article is part of a Special issue entitled: ‘HITRAN 2024’ published in Journal of Quantitative Spectroscopy and Radiative Transfer.

[*] Corresponding authors.
E-mail addresses: erin.adkins@nist.gov (E.M. Adkins), igordon@cfa.harvard.edu (I.E. Gordon).

https://doi.org/10.1016/j.jqsrt.2025.109629
Received 30 April 2025; Received in revised form 8 August 2025; Accepted 8 August 2025
Available online 16 September 2025
0022-4073/Published by Elsevier Ltd.

[7,8] and geometry [9], aerosol profiles [10], as well as temperature profiles [11–13] in limb sounding measurements. While in exoplanetary atmosphere studies, observations of O_2 spectra are expected to be an important biosignature [14,15] in the search for extraterrestrial life and potentially habitable planets.

Because O_2 lacks a permanent electric dipole moment, its interaction with electromagnetic radiation usually involves weakly allowed magnetic dipole transitions, which correspond to the occurrence of unpaired electrons in its ground state [16]. HITRAN includes O_2 magnetic dipole transitions involving the $X^3\Sigma_g^-$ (X) ground state and the $a^1\Delta_g$ (a), $b^1\Sigma_g^+$ (b), $B^3\Sigma_u^-$ (B), $A^3\Delta_u^+$ (A), $c^1\Sigma_u^-$ (c) and $A'\ ^3\Delta_u$ (A') excited electronic states, which are illustrated in the energy level diagrams in Fig. 1. HITRAN also includes electric quadrupole transitions for the $X(v' = 1) \leftarrow X(v'' = 0)$, $a(v' = 0) \leftarrow X(v'' = 0)$, and $b(v' = 0) \leftarrow X(v'' = 0)$ bands, where the upper and ground state vibrational quantum numbers are v' and v'', respectively. From this point forward, when referring to vibrational transitions, we omit the explicit inclusion of the vibrational labels. Transitions in the ground state include spin-only transitions around a frequency of 60 GHz and pure rotational lines with a band maximum intensity near 1.5 THz. Vibrationless magnetic dipole transitions, as well as weak electric quadrupole transitions, involving the triplet ground state $X^3\Sigma_g^-$ and the two lowest-lying electronic states, $a^1\Delta_g$ and $b^1\Sigma_g^+$, occur in the visible and near-infrared regions. The associated line intensities are relatively weak, but nevertheless, they can be important when considering long path lengths of light–matter interaction in atmospheric and planetary observations. The so-called atmospheric bands in the visible and near-infrared (NIR) regions (A, B, γ, δ) correspond to the $b(0,1,2,3) \leftarrow X(0)$, transitions with band centers located at [762 nm, 688 nm, 629 nm, 580 nm], respectively. The NIR band involving $a(0) \leftarrow X(0)$ is referred to as the 1.27 μm band corresponding to its band center. The Noxon band ($b(0) \rightarrow a(0)$), with a band center at 1.91 μm, is typically observed through emission in the terrestrial atmosphere through ozone photochemistry and is included for the first time in HITRAN2024 [17]. Including hot bands, HITRAN2024 includes twelve rovibronic bands of $^{16}O_2$, covering the wavenumber region 5000 cm^{-1} to 18,000 cm^{-1}. Finally, in the wavelength region below 300 nm, HITRAN includes the Schumann-Runge bands $B(v') \leftarrow X(v'')$ and the three Herzberg bands ($A(v') \leftarrow X(0)$, $A'(v') \leftarrow X(0)$, and $c(v') \leftarrow X(0)$), where use of v' or v'' instead of the specific vibrational quanta indicates multiple states are included.

In the remainder of this article, we provide background on the updated HITRAN2024 line list for O_2 [17]. In Section 2.1, we present *ab initio* calculated intensities of rotation-vibration electric quadrupole (E2) absorption lines within the $^{16}O_2(X^3\Sigma_g^-)$ state. These intensities were carried out using a new E2 surface for this ground-electronic state of O_2. In Section 2.2, we provide a description of the line list for the Noxon band, representing the first time that a line list for this band is included in the HITRAN database. Updates to line positions and advanced (beyond Voigt profile) line-shape air-broadening parameters for the $^{16}O_2$ 1.27 μm band are given in Section 2.3, while in Section 2.4, we present recent measurements and *ab initio* calculations of line intensities for the A-band and update line-shape parameters to accurately report air-broadening line-shape parameters. In Section 2.5, we present measured line position and non-Voigt line-shape parameters for the $^{16}O_2$ B-band for self- and air-broadening. Also, in Section 2.6, we address inconsistencies in prior HITRAN editions in the Schumann-Runge (SR) bands and how they have been corrected in HITRAN2024 [17]. Section 2.7 describes the inclusion of CO_2 perturbed collisional broadening parameters for O_2 transitions in HITRAN2024. The article ends with recommendations and an outlook. See Sections 3.1 through 3.5, which respectively discuss the importance of a standard definition for air composition, future updates to the 60 GHz rotational manifold, motivation for improved *ab initio* intensities and measurements, band-to-band variation in line-shape parameters, and higher-order line-shape complications that occur at elevated pressure.

2. Oxygen updates to HITRAN2024 database

The following section of this paper describes the O_2 updates to the HITRAN2024 [17] database by band or by topics which impact the entire O_2 line list. Before discussing these updates, we introduce the conventions for the line-shape parameters and transition nomenclature that will be used throughout the remainder of this work.

The Voigt profile is the standard reference line profile used in HITRAN to model line shapes using four physical parameters (in cm^{-1}): vacuum line center, $\tilde{\nu}_0$, Doppler width, Γ_D, collisionally broadened Lorentzian width, Γ_0 (HITRAN uses half width at half maximum (HWHM) coefficients), and pressure shift of the transition frequency, Δ_0. In recent years, the relational database structure of HITRANOnline has enabled the facile inclusion of advanced line profiles into the HITRAN database [21]. In accordance with the IUPAC recommendation [22], the real component of the complex-valued Hartmann-Tran (HT) profile, $\tilde{\Phi}_{\mathrm{HT}}(\tilde{\nu} - \tilde{\nu}_0; \Gamma_D, \Gamma_0, \Delta_0, \nu_{opt}, \Gamma_2, \Delta_2, \eta)$, [23] has been adopted by HITRAN as the most general beyond-Voigt line profile. This profile includes four additional parameters accounting for higher-order physical effects. These beyond-Voigt parameters are: the frequency of velocity-changing collisions, ν_{opt}, associated with Dicke narrowing in the hard-collision approximation, speed-dependent broadening, Γ_2, and shifting, Δ_2, both based on the quadratic approximation, and correlations between velocity- and state-changing collisions, η [22,23]. Note that Γ_0, Δ_0, ν_{opt}, Γ_2, and Δ_2 are all proportional to pressure, p, with the corresponding pressure-normalized values specified as γ_0, δ_0, $\tilde{\nu}_{opt}$, γ_2, and δ_2, respectively. Note, the speed-dependent parameters are also reported as pressure independent ratios, $a_w = \frac{\gamma_2}{\gamma_0}$ and $a_s = \frac{\delta_2}{\delta_0}$. Table 1 summarizes the line-shape parameters, symbols, units, and their environmental dependencies for HT limiting-case profiles.

Limiting cases of the HT profile effectively correspond to setting one or more of the beyond-Voigt parameters $\boldsymbol{x} = [\tilde{\nu}_{opt}, \gamma_2, \delta_2, \eta]$ to zero. Specifically, the speed-dependent Voigt profile (SDV), ($\boldsymbol{x} = [0, \gamma_2, \delta_2, 0]$) includes only speed-dependence terms, the Nelkin-Ghatak (NG) profile ($\boldsymbol{x} = [\tilde{\nu}_{opt}, 0, 0, 0]$) has only the Dicke narrowing term, whereas the speed-dependent Nelkin-Ghatak (SDNG) profile ($\boldsymbol{x} = [\tilde{\nu}_{opt}, \gamma_2, \delta_2, 0]$) includes both Dicke narrowing and speed-dependent effects with no correlations between the two mechanisms. O_2 spectroscopic reference data included in HITRAN2024 [17] uses the Voigt, SDV, and SDNG profiles (nested under HT profile in HITRAN); therefore, Table 1 does not include the η parameter. Calculations with these parameters are enabled through the HITRAN Application Programming Interface (HAPI) [24], which is a tool that enables downloading the HITRAN data and carrying out calculations of cross-sections, transmittance, etc. Different profiles discussed here are implemented in HAPI, but it also has a “Priority” profile that calculates with HT profile (including SDNG) if the HT parameters are available; in case they are not, it looks for SDV parameters to calculate with SDV profile if available; and finally if no advanced line shape parameters are available, it calculates with Voigt profile, which has parameters for every line in HITRAN. It should also be noted that a new spectroscopic reference profile is being adopted by HITRAN, known as the modified-Hartmann-Tran profile (mHT) [25]. The mHT and HT profiles are equivalent when $\eta = 0$ and share limiting case profiles, such that the O_2 line-shape parameters included in HITRAN2024 [17] are unaffected by the updated line-shape recommendation.

In addition, the first-order Rosenkranz line mixing parameterization can be used with any of the HT limiting-case profiles [26], so that the line shape is modeled as $\Phi(\tilde{\nu}) = \Phi^R(\tilde{\nu}) + Y\Phi^I(\tilde{\nu})$, where Φ^R_{HT} and Φ^I_{HT} are the real and imaginary components, respectively, of $\tilde{\Phi}_{\mathrm{HT}}$ and Y is the line mixing parameter (with $y = Y/p$ being the pressure-normalized value).

O_2 rovibronic transitions are labeled as $\Delta N N'' \Delta J J''$, where N is the quantum number corresponding to the rotational angular momentum ($\mathbf{N}$), S is the quantum number corresponding to the spin angular momentum ($\mathbf{S}$), and J is the total angular momentum quantum number

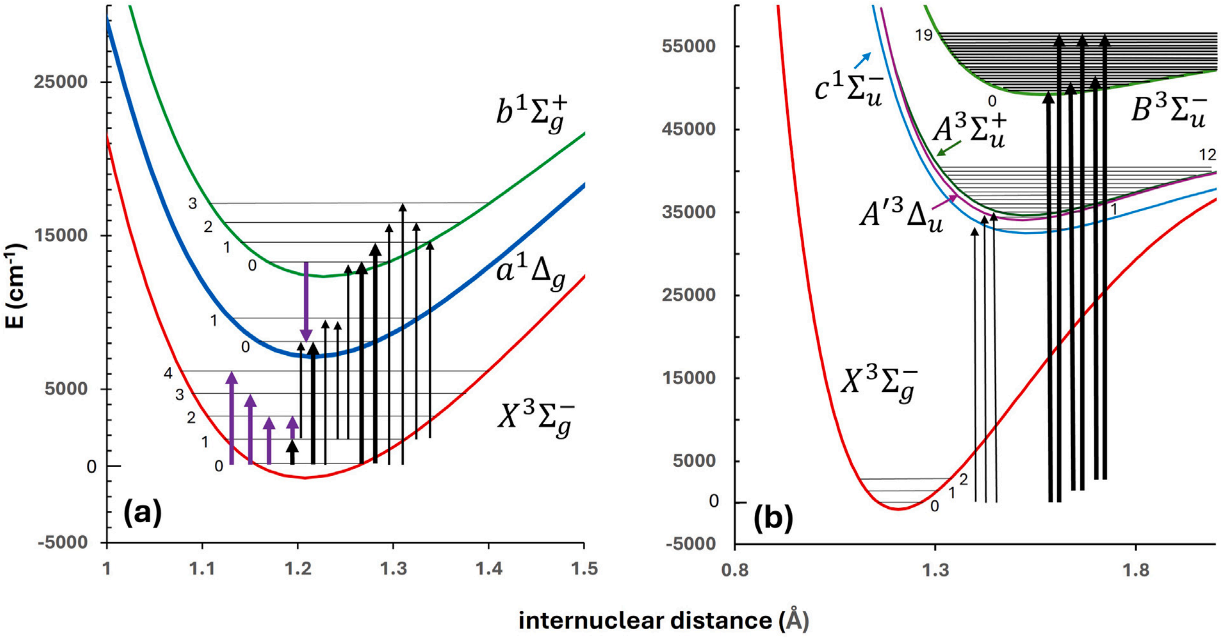

Fig. 1. Energy level diagram for $^{16}O_2$ illustrating the seven involved electronic states and various vibrational and vibronic bands in HITRAN2024. Thick arrows indicate bands for which there are updates in this edition, while purple arrows indicate bands that are being included in HITRAN for the first time in HITRAN2024. (a) Transitions between the indicated vibrational levels involving the ground state, X and two lowest excited electronic states, a and b. Note that the Noxon band is designated by emission ($b(0) \rightarrow a(0)$), while the $X(0) \leftarrow X(0)$ and $X(1) \leftarrow X(1)$ transitions included in HITRAN2024 are not depicted in this figure. (b) Schumann-Runge bands $B(v') \leftarrow X(v'')$ and the three Herzberg bands $A(v') \leftarrow X(0)$, $A'(v') \leftarrow X(0)$ and $c(v') \leftarrow X(0)$, where only the vibrational bands 1 .. 12 in the A state are shown.
Source: Electronic potentials are adapted from [18] (X, a, b), [19] B, and [20] (A, A', c).

Table 1
Line-shape parameter summary for Hartmann-Tran limiting-case line profiles (η = 0). Parameters are tabulated in HITRAN at the reference temperature T_r = 296 K. The environmental dependence column provides the functional form to calculate the parameter at a given pressure (p) and temperature (T). Unless otherwise specified, the text describes parameters at the reference temperature. For simplicity, the broadener is not indicated in this table; however, throughout the text, the collisional broadener is specified by an additional subscript (e.g., $\gamma_{0,\mathrm{air}}$, $\gamma_{0,\mathrm{self}}$).

	Parameter	Units	Environmental dependence
Collisional broadening	γ_0	cm^{-1} atm^{-1}	$\Gamma_0(p,T) = \gamma_0(T_r)p(T_r/T)^{n_{\gamma_0}}$
	n_{γ_0}		
Pressure shifting	δ_0	cm^{-1} atm^{-1}	$\Delta_0(p,T) = p(\delta_0(T_r) + \delta_0'(T - T_r))$
	δ_0'	cm^{-1} atm^{-1}K^{-1}	
Speed-dependent broadening	γ_2	cm^{-1} atm^{-1}	$\Gamma_2(p,T) = \gamma_2(T_r)p(T_r/T)^{n_{\gamma_2}}$
	n_{γ_2}		
	$a_w = \gamma_2/\gamma_0$		
Speed-dependent shifting	δ_2	cm^{-1} atm^{-1}	$\Delta_2(p,T) = p(\delta_2(T_r) + \delta_2'(T - T_r))$
	δ_2'	cm^{-1} atm^{-1} K^{-1}	
	$a_s = \delta_2/\delta_0$		
Dicke narrowing	$\tilde{\nu}_{opt}$	cm^{-1} atm^{-1}	$\nu_{opt}(p,T) = \tilde{\nu}_{opt}(T_r)p(T_r/T)^{n_{\nu_{opt}}}$
	$n_{\nu_{opt}}$		
First-order line mixing	y	atm^{-1}	$Y(p,T) = y(T_r)p(T_r/T)^{n_y}$
	n_y		

($\mathbf{J} = \mathbf{N} + \mathbf{S}$). N'' and J'' refer to the lower states of the respective quantum numbers, while N' and J' refer to the upper states. The Δ values specify the difference between upper and lower state quantum numbers, where values of −2, −1, 0, 1, 2 are labeled as *O, P, Q, R, S*, respectively. This assignment scheme gives rise to branches with differing values of ΔN and subbranches with differing values of $\Delta N \Delta J$. A total angular momentum index, m, is commonly used when discussing P- and R-branch O_2 transitions, where $m = -J''$ for the P-branch and $m = J'' + 1$ for the R-branch. For example, a P3Q2 transition would be in the P-branch and PQ-subbranch, with $N'' = 3$, $J'' = 2$, and $m = -2$.

2.1. Electric quadrupole line intensities of rovibrational transitions in the $X^3\Sigma_g^-$ electronic term of $^{16}O_2$

In Ref. [27], the intensities of all rovibrational electric quadrupole (E2) absorption lines in $^{16}O_2(X^3\Sigma_g^-)$ corresponding to vibrational quantum numbers $v \le 35$ and total angular momentum quantum numbers $J \le 40$ were calculated using a new *ab initio* E2 transition moment curve of the ground-electronic O_2. The calculations were performed in the intermediate coupling case, i.e., using the exact eigenfunctions of the effective Hamiltonian of $^{16}O_2(X^3\Sigma_g^-)$, which means going beyond the simple Hund's case (b) approximation and including the rotational state-mixing induced by the relativistic electronic spin-spin interaction. This results in the occurrence of additional rotational branches that cannot be accounted for otherwise.

The transition moments, necessary for computing the absorption intensities, were obtained using a new *ab initio* E2 moment curve of the ground-electronic O_2, taking the full bond-length dependence of the molecular E2 tensor into account. The curve was calculated with the multi-reference configuration interaction (MRCI) method using MOLPRO v2022.22 [28], employing the uncontracted d-aug-cc-pV6Z basis set [29] with all electrons distributed among the 10 lowest molecular orbitals. The calculations were performed in the 0.70–3.50 Å range of internuclear O-O distances (with a constant step of 0.01 Å), with an estimated uncertainty of ∼10% [27]. The relevant matrix elements of the E2 moment curve were obtained using the rovibrational wave functions calculated with the discrete variable representation (DVR) method [30,31] using the potential energy function of $^{16}O_2(X^3\Sigma_g^-)$ reported by Bytautas, Matsunaga and Ruedenberg [32]. The DVR calculations employed 500 basis functions and were performed across 2000 evenly spaced points in the 0.5–10.0 a_0 range of internuclear O-O distances. To ensure that the wave functions satisfied the orthogonality conditions with sufficient numerical accuracy, all calculations were performed using quadruple precision. Following previous works on electric dipole transitions in other molecules [33–38], when calculating the relevant transition moment integrals, the E2 moment curve was represented using a single, continuously defined analytic function (Padé function) fitted to the *ab initio* points, as opposed to piecewise-defined spline interpolation, to ensure that the so-called “natural intensity distribution law” [39] is satisfied. The “natural intensity distribution law” relates to the asymptotic high-frequency behavior of the calculated transition moments. In the case of rovibrational E2 transitions in $^{16}O_2(X^3\Sigma_g^-)$, using a non-analytic spline interpolation for the E2 moment curve results in an unphysical saturation of the absorption intensities for high vibrational overtones (as a function of the final-state vibrational quantum number) around a constant value [27]. This observation agrees with the findings of previous works [33–38] that considered electric dipole spectra in molecules other than oxygen.

HITRAN2020 [40] included the data on the E2 absorption lines in $^{16}O_2(X^3\Sigma_g^-)$ only for the $X(1) \leftarrow X(0)$ fundamental vibrational band. Gancewski et al. [27] considered all fine-structure resolved rovibrational E2 transitions (within the ground-electronic term) for which the vibrational and the total angular momentum quantum numbers were, respectively, $v \leq 35$ and $J \leq 40$. This resulted in 666 vibrational bands (both overtone and hot bands) comprising a total of 280 188 individual spectral lines, provided in the supplementary material of Ref. [27]. For practical use in the terrestrial-atmospheric radiative transfer codes, this line list has been truncated according to a 10^{-33} cm/molecule intensity cutoff, resulting in 1148 lines included in the new 2024 edition of HITRAN [17], corresponding to the pure-rotational ($X(0) \leftarrow X(0)$), fundamental ($X(1) \leftarrow X(0)$), overtone ($X(2,3,4) \leftarrow X(0)$) and hot $X(2,1) \leftarrow X(1)$) vibrational bands. Fig. 2 shows these *ab initio* absorption intensities (black points) alongside the aforementioned HITRAN2020 [40] data (red points). The relevant absorption intensities were calculated at the HITRAN reference temperature $T_r = 296$ K. For convenience, the temperature-independent Einstein *A*-coefficients for these transitions were also reported in Ref. [27]. The energy levels required for computing the associated transition frequencies and the Boltzmann probabilities, as well as the molecular constants of the effective Hamiltonian used for determining the rotational state-mixing coefficients, were taken from Yu et al. [18]. The relative difference between the *ab initio* intensities [27] and those available in HITRAN2020 [40] for the $X(1) \leftarrow X(0)$ band fall within a range of 5% to 12%, depending on the fine-structure resolved rotational transition [27].

Besides the E2 absorption lines, the HITRAN2020 [40] data on the $X(1) \leftarrow X(0)$ band also included the magnetic dipole (M1) transitions. Therefore, it is worth commenting on the relative intensities of the E2 and M1 lines in the fundamental band of $^{16}O_2(X^3\Sigma_g^-)$. For transitions satisfying common selection rules $\Delta J = 0, \pm 1$, the M1 components are, in general, much stronger than their E2 counterparts (explicit comparison for all rotational branches can be found in Ref. [27]). In this context, it is interesting to note, however, that the $F_2 \leftarrow F_2$ fine-structure resolved component of the rotational *Q*-branch exhibits the opposite behavior, namely that the corresponding M1 intensities are orders of magnitude smaller than those of the E2 components. Note, the $F_f \leftarrow F_i$ notation used for denoting fine-structure resolved rotational transitions is explained in detail in Ref. [27]. In this case, the mechanism responsible for the relative weakness of the M1 absorption lines was expounded upon by Balasubramanian, Bellary and Rao [41] and is associated with the partial cancellation of matrix elements of the magnetic dipole operator for transitions between different vibrational levels. This atypical (for O_2) behavior is shown in Fig. 3.

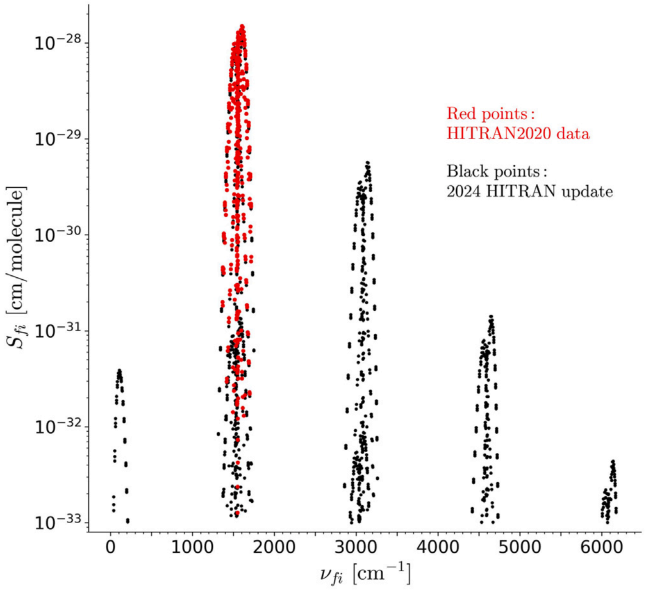

Fig. 2. Comparison between the new *ab initio* electric quadrupole absorption intensities of rovibrational $^{16}O_2(X^3\Sigma_g^-)$ lines [27] included in HITRAN2024 [17] (black) and those available in HITRAN2020 [40] (red) as a function of transition wavenumber. The new *ab initio* data comprises 1148 lines, including the pure-rotational ($X(0) \leftarrow X(0)$), fundamental ($X(1) \leftarrow X(0)$), overtone ($X(2,3,4) \leftarrow X(0)$) and hot ($X(2,1) \leftarrow X(1)$) vibrational bands, while the previous HITRAN [40] edition includes only the $X(1) \leftarrow X(0)$ fundamental band. Note that the M1 transitions are not shown on this plot.

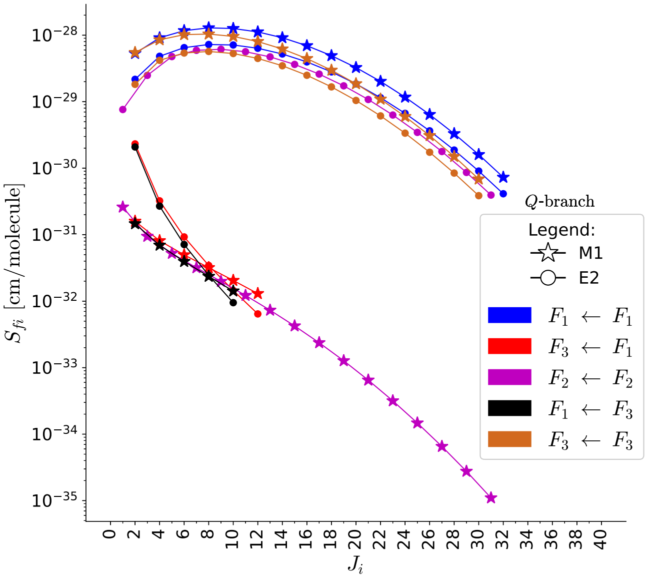

Fig. 3. Magnetic dipole (stars, M1) and electric quadrupole (circles, E2) spectral line intensities for the rotational *Q*-branch of the $X(1) \leftarrow X(0)$ fundamental vibrational band in $^{16}O_2(X^3\Sigma_g^-)$ as a function of the initial-state total angular momentum quantum number. The different colored curves correspond to various fine-structure resolved transitions (specified in the plot legend). It can be seen that the M1 lines are, in general, stronger than their E2 counterparts, with the notable exception of the $F_2 \leftarrow F_2$ fine-structure resolved *Q*-branch component (magenta). Although atypical for O_2, this behavior was explained in Ref. [41] on the basis of partial cancellation of matrix elements of the magnetic dipole operator.

2.2. Noxon band: $b^1\Sigma_g^+(0) \rightarrow a^1\Delta_g(0)$

Transitions between the $a^1\Delta_g$ and $b^1\Sigma_g^+$ states are possible only through the electric quadrupole mechanism. Considering that the thermal population of the $a^1\Delta_g$ state cannot be achieved under terrestrial conditions, these transitions are typically observed in emission when the oxygen molecules (that are created in the $b^1\Sigma_g^+$ state through ozone photochemistry) emit light upon transitioning to the $a^1\Delta_g$ state. These transitions were first identified by Noxon [42], and hence are referred to by that name. The line positions were calculated using the $a^1\Delta_g(0)$ band constants reported in Ref. [43] and those of the $b^1\Sigma_g^+(0)$ state from Ref. [18]. The intensities were calculated using the quadrupole moment determined experimentally by Ionin et al. [44]. For this band, the intensities in the HITRAN formalism of thermal equilibrium are much smaller than the intensities of any other bands of oxygen in HITRAN. When calculating emission in this band, one should not assume that the state populations are in thermal equilibrium. See discussion in Refs. [13,45] on the modeling of oxygen airglow in different bands.

2.3. *Oxygen 1.27* μm *band:* $a^1\Delta_g \leftarrow X^3\Sigma_g^-$

2.3.1. *Line intensities and line centers*

Updated line positions and line intensities were included in HITRAN2020 [40] for the 1.27 μm band. However, the paper describing that work is still in preparation with an aim for publication in 2026 [43]. The line intensities in HITRAN2024 [17] are consistent with those reported in HITRAN2020 [40] and described in Gordon et al. [43]. The 1.27 μm band line positions for $^{16}O_2$ and $^{16}O^{18}O$ reported in HITRAN2020 [40] were a preliminary fit of the work reported in [43], which are included in HITRAN2024 [17]. Both the 1.27 μm band line center and line intensity updates are briefly described below.

Line positions for the 1.27 μm band are updated in HITRAN2024 [17] to values calculated in Gordon et al. [43] from simultaneous fits to determine spectroscopic constants for the upper state, $a^1\Delta_g$ (0, 1) and lower state $X^3\Sigma_g^-$ (0, 1). The fit included optical frequency comb (OFC) referenced line positions measurements from Université Grenoble Alpes (Grenoble) [43,46,47], and National Institute of Standards and Technology (NIST) [48], along with additional microwave and IR transition measurements [16,49–57]. The comb-referenced measurements improved the accuracy of the fit spectroscopic constants, resulting in line positions with uncertainties less than 10^{-5} cm^{-1}.

The intensities of the measurements in Grenoble [43,46,47] and NIST [48] were fit to a model where the electric quadrupole (E2) contributions were properly accounted for, therefore enabling not only modeling the purely E2 transitions $\Delta J = \pm 2$, but also disentangling M1 and E2 contributions for the overlapping lines with $\Delta J = 0, \pm 1$ [43]. This is important considering the sub-percent level of accuracy demanded by the atmospheric missions. The relative contribution of the electric quadrupole lines (in comparison with much stronger magnetic dipole lines) in the 1.27 μm band is more pronounced than that in the A-band. This is due to the mixing of the $b^1\Sigma_g^+$ and $\Omega = 0$ components of the ground $X^3\Sigma_g^-$ state. This mixing allows borrowing of the intensities from the Noxon band, which is purely electric quadrupole as it is between $a^1\Delta_g$ and $b^1\Sigma_g^+$ states. Because $\Omega = 0$ is a component of only two out of three spin-components in the ground states, the electric quadrupole transitions contribute appreciably only to some of the subbranches. However, there is a very weak mixing of the $\Omega = 1$ component in the ground state with the much higher lying (in energy) $^1\Pi$ electronic state, allowing for the very weak E2 contribution. Interestingly, thanks to the sensitivity of the experiments carried out in Grenoble [43,47], this contribution was determined experimentally by measuring OO ($\Delta N = -2, \Delta J = -2$) and SS ($\Delta N = 2, \Delta J = 2$) lines. The modeling of magnetic dipole lines required introducing the Hermann-Wallis-like corrections, which were different for the subbranches that involved different spin-components in the ground state. Overall, nine M1 subbranches and fifteen E2 subbranches were added for this band in HITRAN, with the intensity cut-off 10^{-32} cm/molecule.

2.3.2. *Line-shape parameters and temperature dependencies*

In recent years, a number of studies have been dedicated to the determination of the line-shape parameters of the rovibronic transitions of the 1.27 μm band of O_2 in air. The comb-referenced cavity ring-down spectroscopy (CR-CRDS) [58,59] and the frequency-agile, rapid scanning (FARS-CRDS) [60] approaches have been used by groups at Grenoble and NIST, respectively, to circumvent the weakness of the intensity of the considered magnetic dipole transitions and to record spectra with signal-to-noise ratios of a few thousand or more. Two studies have been carried out at room temperature, one at Grenoble [46] and the other at NIST [48]. After applying a multi-spectrum fit procedure with the SDNG profile [23], they each provided a set of line-shape parameters at 296 K. The line-mixing effect, in its first-order approximation [26], was also included when necessary. The retrieved profile parameters are the air-broadening and the air-pressure shift coefficients, their speed dependence components, the Dicke narrowing parameter, and the first-order line-mixing coefficient (outlined in Table 1). The measurements made in Grenoble were extended to 253 K, 275 K, and 333 K for 55 lines by using a temperature-regulated high finesse cavity [61]. In this latter study, the line-shape parameters at 296 K and their temperature dependence coefficients/exponents were retrieved. Table 2 summarizes the observations at NIST and Grenoble [46,48,61].

In HITRAN2020 [40], the Voigt line-shape parameters were obtained from Voigt profile analyses of the Grenoble spectra reported in Tran et al. [46]. This Voigt profile line list has not been updated for HITRAN2024 [17]. However, it is well known that the Voigt profile does not allow for the precise reproduction of the observed line profiles (see Fig. 5 in Fleurbaey et al. [48]), leading to effective parameters which are noticeably different than those obtained with the SDNG profile (up to 4% for $\gamma_{0,\mathrm{air}}$ [61]). For the advanced line-shape parameter update in HITRAN2024 [17], the SDNG line-shape parameters at 296 K and their temperature dependencies (including first-order line-mixing), are generated by combining the results of Fleurbaey et al. [48] and Klemm et al. [61], which are in good agreement at 296 K (see [61] for the detailed comparison), thus mutually validating the accuracy of these independent studies. It is important to mention that the SDNG profile is not explicitly provided in HITRAN, and the parameters for this profile are being nested under HT profile with η set to zero.

Inspection of the measured line-shape parameters suggested that N' is the optimal dependent variable to model measured values for extrapolation in order to minimize the branch dependence of the line-shape parameters. Subbranch differences are still observed in N'-dependent modeling of the line-shape parameters [61]. For this reason, the SDNG line-shape parameters included in HITRAN2024 [17] are the measured values when available and extrapolated values when measurements from NIST or Grenoble were not available. The included temperature dependencies of the line-shape parameters are the values modeled from fits to the measured values reported in [61] for all transitions. For the measured branches, values were extrapolated to $N'' = 49$. The parameter values and extrapolation functions are provided in Table 3. The uncertainties reported in HITRAN2024 [17] for the measured parameters correspond to the reported measurement uncertainties from Klemm et al. [61] and Fleurbaey et al. [48]. For the interpolated and extrapolated parameters, we report the one standard deviation confidence interval [62] added in quadrature with the standard deviation in the fit residuals for the parameter (available in the Supplementary Materials). The measurements reported by Fleurbaey et al. [48] and Klemm et al. [61] span temperatures from 253 K to 333 K. It is believed that the temperature dependence coefficients/exponents provided in this HITRAN2024 [17] are reasonably valid over the 230–350 K temperature range. The minor isotopologues will adopt the line-shape parameter values of $^{16}O_2$.

It should be noted that the HITRAN2020 publication [40] mentioned including the Fleurbaey et al. [48] advanced line-shape parameters and first-order line-mixing, however, these parameters were mistakenly omitted from the HITRAN2020 [40] release through the HITRAN server. Additionally, as we combine studies from Grenoble and NIST for advanced line-shape parameter inclusion in the HITRAN2024 database, it is important to note that in Fleurbaey et al. [48] the reported line-shape parameters were mistakenly indicated to have units of kHz/kPa, where the reported numerical values were actually in units of kHz/Pa.

For the 53 transitions measured by both Fleurbaey et al. [48] and Klemm et al. [61], the $\gamma_{0,\mathrm{air}}$ and $\delta_{0,\mathrm{air}}$ values at 253 K, 275 K, 296 K, and 333 K were used as inputs in fits to the environmental dependencies (outlined in Table 1) to determine $\gamma_{0,\mathrm{air}}$, $n_{\gamma_{0,\mathrm{air}}}$, $\delta_{0,\mathrm{air}}$, and $\delta'_{0,\mathrm{air}}$, where

Table 2
Summary of recent 1.27 μm band line-shape parameter studies conducted in Grenoble and at NIST included in the HITRAN2024 update.

Group	Ref.	Spectral region (cm^{-1})	No. of lines	$N'_{\max}$	Temperature (K)
NIST	Fleurbaey et al. [48]	7797–7953	99	30	~296.3
Grenoble	Tran et al. [46]	7720–7920	85	29	~294.3
Grenoble	Klemm et al. [61]	7730–7940	55	29	253, 275, 333

the determined $\gamma_{0,\text{air}}$ and $\delta_{0,\text{air}}$ for these transitions are included in HITRAN2024. Of the 46 transitions measured only in Fleurbaey et al. (at 296 K), the $\gamma_{0,\text{air}}$ and $\delta_{0,\text{air}}$ values are those from Fleurbaey et al. [48]. A fit versus N′ to the data reported by Klemm et al. [61] (55 transitions) and Fleurbaey et al. [48] (46 transitions measured only at NIST) was used to interpolate $\gamma_{0,\text{air}}$ and $\delta_{0,\text{air}}$ values for transitions that were not among the observations of [48,61], and to extrapolate beyond available measurements to $N'' = 49$. A Padé approximant was used to model $\gamma_{0,\text{air}}(N')$ (see Table 1). The pressure shifting term was modeled by:

$$\delta_{0,\text{air}}(N') = \alpha_1 + \alpha_2 e^{-N'\beta_2}. \tag{1}$$

Eq. (1) is a simplified version of the empirical form proposed by Hartmann to model pressure shifts across multiple vibrational bands of carbon dioxide [63]. A different simplification of this form is also used to model the O_2 B-band air-broadened pressure shifts and is discussed in an upcoming section. Because the $\delta_{0,\text{air}}$ branch dependencies are significant, each branch (*O, P, Q, R*, and *S*) was modeled separately. Table 3 summarizes the model functions and fit parameters used for modeling the 1.27 μm band line-shape parameters, while Figs. 4 and 5 depict the air-broadening advanced line-shape parameters for the 1.27 μm band included in HITRAN2024 [17].

For all transitions, the $n_{\gamma_{0,\text{air}}}$ values correspond to those provided by a Padé approximant fit of the N' dependence reported in Table 3 based on the 53 temperature exponents obtained for transitions measured by both Fleurbaey et al. [48] and Klemm et al. [61]. It is important to mention that the $n_{\gamma_{0,\text{air}}}$ values reported in HITRAN2020 [40] were in good agreement with new measurements only for transitions where $N' \leq 10$. For transitions with larger N' values, the new temperature exponents decrease much faster than the HITRAN2020 values (see Fig. 5 of Klemm et al. [61]). Hence, considering transitions with $N' = 18$, the use of the HITRAN2020 temperature dependence exponent leads to a difference of 0.5% for the air-broadening coefficient at 273 K, which increases to 1.4% for transitions with $N' = 24$.

The temperature dependence of the pressure shifting term shows a clear subbranch dependence. The $\delta'_{0,\text{air}}$ coefficient for all transitions is provided by a second-order polynomial fit *versus* N' (up to $N' = 29$) of the $\delta'_{0,\text{air}}$ values for each subbranch (obtained using both [48,61]). For $\delta'_{0,\text{air}}$ values beyond the measured transitions, $\delta'_{0,\text{air}}$ is fixed to a constant value equal to the modeled value for the last measured transition in the subbranch, typically about 8.0×10^{-6} $cm^{-1}atm^{-1}K^{-1}$. Because of the small number of measured *SR*-subbranch transitions, the same model parameters are used for the *SR*-subbranch and the *RQ*-subbranch.

The Dicke narrowing, speed-dependent broadening, and speed-dependent shifting parameters were determined from the average of the Fleurbaey et al. [48] and Klemm et al. [61] values for the 55 common transitions and the Fleurbaey et al. [48] values for the 46 transitions only measured at NIST. The parameters were each modeled using a Padé approximant, as outlined in Table 3, to extrapolate beyond the measured transitions.

For the temperature exponent of $\tilde{\nu}_{opt,\text{air}}$, no significant N' dependence is observed, and a value of 1.9 is adopted for $n_{\nu_{opt,\text{air}}}$ for all reported transitions, as suggested by Klemm et al. [61]. In Klemm et al. [61], no clear N' tendency was evidenced for $n_{\gamma_{2,\text{air}}}$. Following this reference, values of 0.46 for $N' \leq 6$ and 0.13 for $N' > 6$ are adopted for $n_{\gamma_{2,\text{air}}}$. In Klemm et al. [61], no clear temperature dependence was evidenced for $\delta_{2,\text{air}}$ and the temperature dependence parameter ($\delta'_{2,\text{air}}$) is fixed to zero for all N' values.

Line-mixing has been observed for six of the nine subbranches and is clearly subbranch-dependent [61]. The line-mixing coefficients for air included in HITRAN2024 [17] are the average of measurements from Fleurbaey et al. [48] and Klemm et al. [61]. Unlike other reported line-shape parameters, line-mixing terms are not interpolated or extrapolated beyond available measurements or for lines where fits constrained the line-mixing to be zero. The results reported in Klemm et al. [61], determined a mean value of 1.45(35) for $n_{y_{\text{air}}}$, which is adopted in HITRAN2024 for the line-mixing temperature dependence exponent for the lines with measured non-zero line-mixing coefficients [17]. For the 1.27 μm band, no attempt to satisfy the sum rules has been made for the line-mixing coefficients in HITRAN2024. Future studies would benefit from exploring the use of either the exponential power gap model or energy corrected sudden scaling law to model measured line-mixing coefficients in a way that satisfies the detailed population balance.

2.4. Oxygen A-band: $b^1\Sigma_g^+(0) \leftarrow X^3\Sigma_g^-(0)$

The main O_2 A-band update in HITRAN2024 [17] is to the line intensities. However, the line-shape parameters have also been revised to account for a compilation oversight that led to N_2 broadening line-shape parameters, originally published in Ref. [6], being included as air-broadening parameters in HITRAN2020 [40]. This error has been corrected for the Voigt and SDV line-shape parameters in HITRAN2024 [17]. On average the air collisional broadening parameters are about 2% larger than the N_2 collisional broadening parameters in the O_2 A-band. The reported air-broadening parameters have been calculated assuming an O_2 amount fraction of 0.21 in a balance of N_2. In the multi-spectrum fits by Payne et al. the a_w values were assumed to be independent of the collisional partner [6]. In HITRAN2024 [17], $\gamma_{2,\text{air}}$ and $\gamma_{2,\text{O2}}$ are calculated as $a_w\gamma_{0,\text{air}}$ and $a_w\gamma_{0,\text{O2}}$, respectively. The air-broadened line-mixing parameters reported in HITRAN2020 were not subject to this discrepancy, so they have remained consistent between HITRAN2020 [40] and HITRAN2024 [17]. The recommendations and outlook section of this work contains a related discussion on the impact of the definition of air, in terms of amount fraction and inclusion of air-component species, when reporting air-broadening parameters for O_2 bands.

The HITRAN2024 [17] O_2 A-band line intensities are based on frequency agile rapid scanning cavity ring-down spectroscopy (FARS-CRDS) measurements of 72 $^{16}O_2$ A-band transitions up to $J = 40$ modeled and extrapolated to $J = 60$ using scaled *ab initio* intensity calculations [64]. These measurements reduced uncertainties in the O_2 A-band line intensities by addressing several key factors that were likely sources of measurement bias in previous HITRAN O_2 A-band updates. Also, the rotational dependence of the line intensities was modeled with *ab initio* calculations [65], thus capturing more of the underlying physics than was previously available using conventional intensity models [66,67]. We will first describe the recent intensity measurements and *ab initio* scaling model before comparing these results to O_2 A-band intensities included in previous HITRAN editions.

The theoretical results reported by Somogyi et al. [65] were the first *ab initio* calculations of the O_2 A-band to be scaled by measured values. This scaling of *ab initio* band intensities is similar to that implemented by Long et al. [68] and Fleurbaey et al. [69] to model the J-dependence of CO_2 intensities in the bands near 1.6 μm and

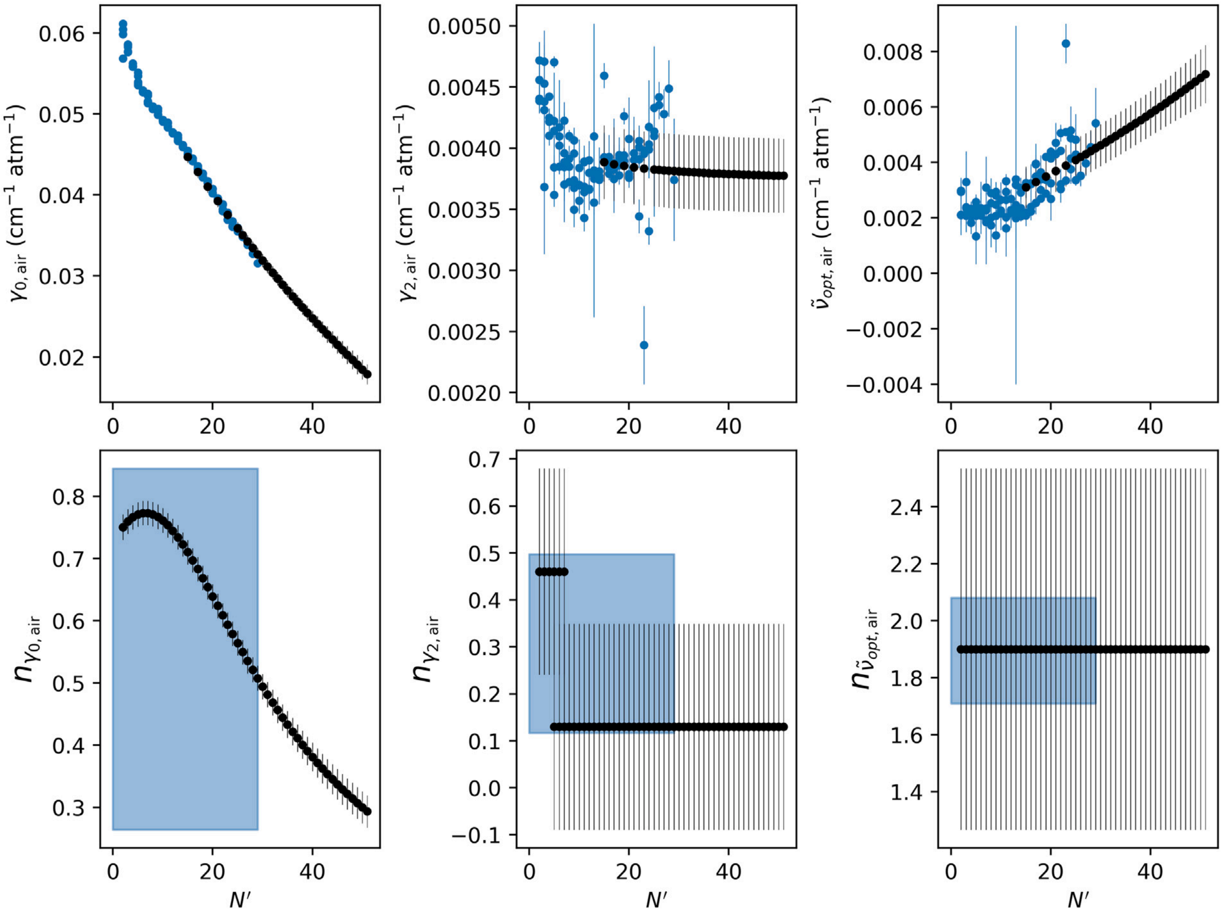

Fig. 4. Air-perturbed pressure broadening, speed-dependent broadening, and Dicke narrowing parameters and their temperature dependencies versus N' for the O_2 1.27 μm band. Colored points represent the measured parameters, and the black points represent the extrapolated parameter values (as summarized in Table 3) included in the HITRAN2024 update [17]. All temperature dependence parameters are based on the reported empirical functions; the shaded regions represent the N'-region where measurements were available.

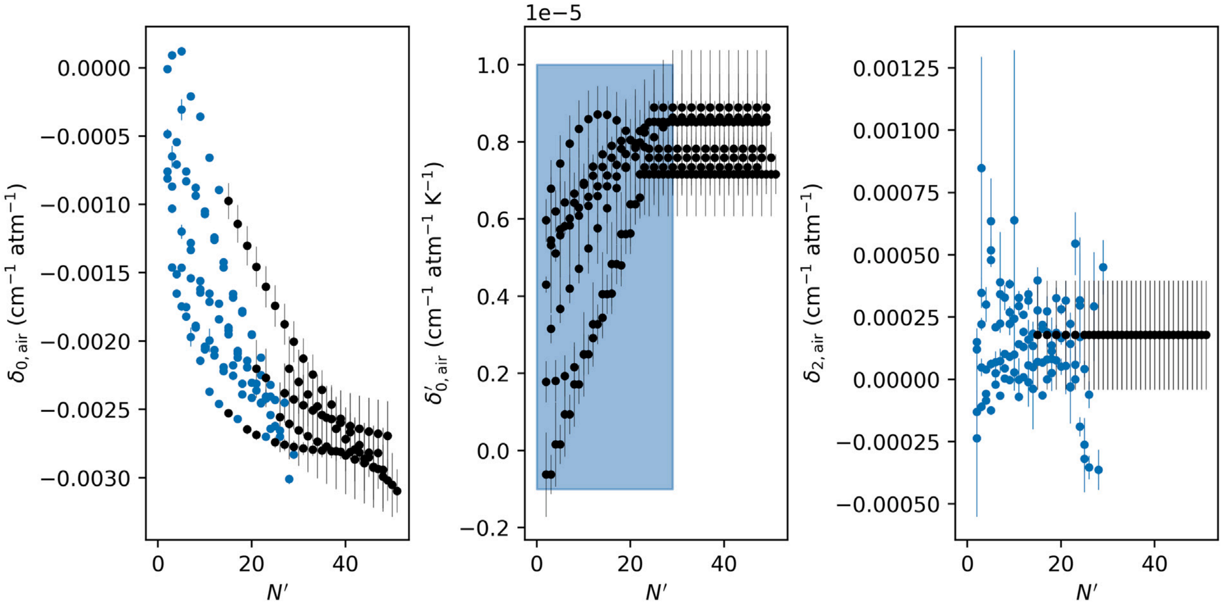

Fig. 5. Air-perturbed collisional shifting and temperature dependence and speed-dependent shifting parameters versus N' for the O_2 1.27 μm band. Colored points represent the measured parameters, and the black points represent the extrapolated parameter values (as summarized in Table 3) included in the HITRAN2024 update [17]. The temperature dependence parameters are based on the reported empirical functions, the shaded regions represent the N'-region where measurements were available.

2.06 μm, respectively. These results were incorporated in HITRAN2020 [40]. For the O_2 A-band, the J- dependencies of the *ab initio* and measured intensities are in excellent agreement for the *PQ*- and *RQ*-subbranches with a standard deviation in the residuals of 0.04% for

Table 3

1.27 μm band of O_2 in air: Expressions and parameters fitted to the experimental values obtained for the line-shape parameters and their temperature dependence exponents/coefficients. Uncertainties in parameters determined using extrapolation functions are provided in the supplementary materials. Line mixing parameters in HITRAN2024 for the 1.27 μm band are based on the average values reported in [48,61] for each transition and are not modeled by an expression (see supplemental materials or HITRAN2024 for values).

	$(c_0 + c_1 N')/(1 + d_1 N' + d_2 (N')^2)$			
	c_0	c_1	d_1	d_2
$\gamma_{0,\mathrm{air}}$ ($\mathrm{cm^{-1}\ atm^{-1}}$)	0.06078	-6.88×10^{-4}	8.58×10^{-3}	0
$n_{\gamma_{0,\mathrm{air}}}$ [a]	0.725	0.0126	-2.75×10^{-3}	1.46×10^{-3}
$\gamma_{2,\mathrm{air}}$ ($\mathrm{cm^{-1}\ atm^{-1}}$)	4.79×10^{-3}	1.35×10^{-3}	0.363	0
$n_{\gamma_{2,\mathrm{air}}}$	0.45 for $N' \le 6$	0	0	0
	0.13 for $N' > 6$	0	0	0
$\delta_{2,\mathrm{air}}$ ($\mathrm{cm^{-1}\ atm^{-1}}$)	1.78×10^{-4}	-2.53×10^{-6}	0	0
$\delta'_{2,\mathrm{air}}$ ($\mathrm{cm^{-1}\ atm^{-1}\ K^{-1}}$)	0	0	0	0
$\tilde{\nu}_{opt,\mathrm{air}}$ [a] ($\mathrm{cm^{-1}\ atm^{-1}}$)	1.79×10^{-3}	7.40×10^{-5}	-4.42×10^{-3}	0
$n_{\nu_{opt,\mathrm{air}}}$	1.9	0	0	0
$n_{y,\mathrm{air}}$	1.45	0	0	0
$\delta_{0,\mathrm{air}}$ ($\mathrm{cm^{-1}\ atm^{-1}}$)	$\alpha_1 + \alpha_2 e^{-N'\beta_2}$			
Branch	α_1	α_2	β_2	
O	−0.002822	0.00202	0.1282	
P	−0.003222	0.001911	0.0429	
Q	−0.003508	0.002807	0.0397	
R[a]	−0.004142	0.003912	0.0255	
S[a]	−0.004821	0.005371	0.0223	
$\delta'_{0,\mathrm{air}}$ ($\mathrm{cm^{-1}\ atm^{-1}\ K^{-1}}$)	$A + B_1 N' + B_2 (N')^2$			
Subbranch	A	B_1	B_2	
OP	4.59124	0.52206	−0.01647	
PP	5.62079	0.11581	0	
PQ	2.91543	0.49936	−0.01212	
QP	5.03983	0.13933	0	
QQ	4.94572	0.12716	0	
QR	2.36915	0.26104	0	
RQ	−1.01164	0.38948	0	
RR	1.80564	−0.03695	0.01254	
SR	−1.01164	0.38948	0	

[a] Indicates that a fictitious data point was added at $N' = 50$ to prevent divergence in extrapolated values.

$J < 30$. However, the *PP*- and *RR*-subbranches exhibit a slight linear deviation (0.14% for $J < 30$) about the band center, which exceeds the statistical uncertainties of the measurements. These differences can be ascribed to subbranch-dependent variations in various intensity components arising from quadrupole, spin–orbit, and electronic angular momentum (L-uncoupling) and other contributions to be addressed in the future by more general *ab initio* calculations [64].

An empirical correction to the relative theoretical intensities in the *PP*- and *RR*-subbranches was included in the *ab initio* intensity scaling model by using a constrained fitting procedure anchored by the J-dependence of the theoretical intensities in the *PQ*- and *RQ*-subbranches. The scaling parameter, β, was determined by fitting Eq. (2) to the measured line intensities, S_m, in the *PQ*- and *RQ*-subbranches. The measured *PP*- and *RR*-subbranch intensities were modeled by Eq. (3), where the linear correction term, b, accounted for the slight difference in the relative magnitudes of the measured and theoretical intensities, $S_{m,ai}$, in these subbranches. Therefore, the *PQ*- and *RQ*-subbranches were modeled by,

$$S_m = \beta S_{m,ai}, \tag{2}$$

whereas the *PP*- and *RR*-subbranches were described as,

$$S_m = \beta S_{m,ai}(1 + bm). \tag{3}$$

Figure 6 shows the results of scaling the *ab initio* intensities to the measured intensities including the empirical correction to the theoretical intensities in the *PP*-and *RR*-subbranches. Introducing this correction decreases the standard deviation in the residuals to 0.04% for all subbranches (for $J < 30$). The band intensity is determined by extrapolating the scaled *ab initio* model to $J = 60$ and summing the intensities, resulting in a band intensity of 2.2496×10^{-22} cm molecule^{-1} with a relative combined standard uncertainty of 0.14%. This uncertainty includes the model uncertainty (between 0.004% and 0.03%) as well as the line-by-line systematic experimental uncertainties (between 0.08% and 0.20%).

HITRAN updates to the O_2 A-band line intensities have long involved pairing the best available experimental data to determine the band intensity with the best available models to describe the J-dependence of the intensities. Table 4 outlines the combination of measurements and models that contributed to the HITRAN editions from 1996 to 2024 [40,70–75], while Fig. 7 compares the J-dependencies (left panel) and band (right panel) intensities from past HITRAN updates to the current version.

Measurements of O_2 A-band line intensities that have contributed to HITRAN editions include those based on tunable dye laser (TDL) experiments [76] and grating spectrometers [77,78] in HITRAN1996 - HITRAN2004 [70–72], frequency-stabilized cavity ring-down spectroscopy (FS-CRDS) investigations [68,80,81] in HITRAN2008 [73] and HITRAN2012 [74], and finally a combination of Fourier transform spectroscopy (FTS) observations [6,82] and FS-CRDS [6,80] techniques in HITRAN2016 [75] and HITRAN2020 [40]. The band intensities reported in these versions differ at about the 1% level. Thus, applications demanding significantly improved accuracy require new line intensity measurements with substantially reduced biases and uncertainties.

Many of these measurements [6,68,76,80–82] spanned a wide pressure range in order to provide line intensities along with line-shape parameters and in some cases parameters for higher-order collisional effects [6,82]. Recent studies have shown that treatment of these higher-order effects (e.g., line mixing, CIA, and intensity depletion) can affect the measured line intensity [6,83–85]. By limiting measurements to the low-pressure domain (<1.35 kPa), the recent measurements reported in Adkins et al. [64], and included in HITRAN2024 [17],

Table 4
Summary of O_2 A-band line intensity measurements and models contributing to HITRAN editions. Acronyms are as follows: tunable diode laser (TDL), frequency-stabilized cavity ring-down spectroscopy (FS-CRDS), Fourier-transform spectroscopy (FTS), and frequency agile rapid-scanning cavity ring-down spectroscopy (FARS-CRDS), Herman-Wallis- modified Watson model (HWW).

HITRAN edition	Line intensity measurements	Line intensity model
1996–2004 [70–72]	TDL [76], grating spectrometer [77,78]	Watson [79]
2008 [73]	FS-CRDS [80]	Watson [79]
2012 [74]	FS-CRDS [68,80,81]	HWW [68]
2016 [75]	FTS [82], FS-CRDS [80]	HWW [68]
2020 [40]	FTS [6,82], FS-CRDS [6,80]	HWW [6]
2024 [17]	FARS-CRDS [64]	*ab initio* scaled [64,65]

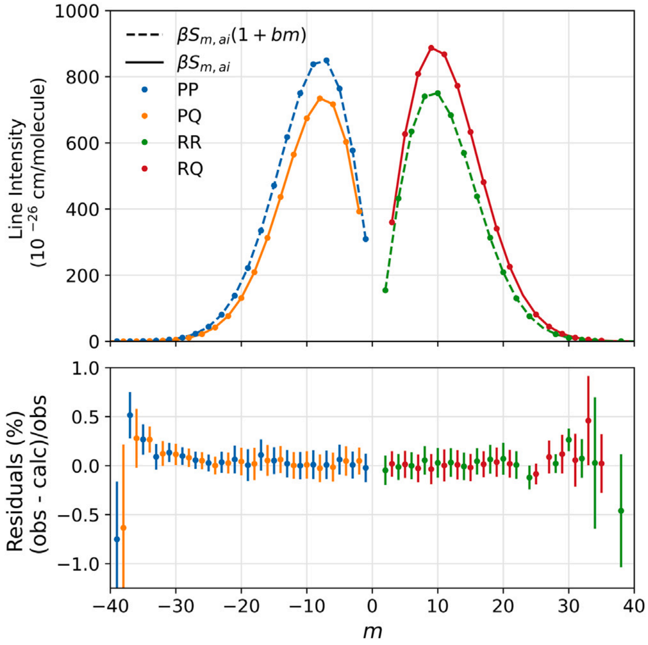

Fig. 6. Model and residuals for *ab initio* intensities scaled by β (*PQ*- and *RQ*-subbranches) and those scaled by β with a linear correction b (*PP*- and *RR*-subbranches) after fits to measured intensities, where β = 0.87981(4), $b = 8.90(54)\times10^{-5}$. Top panel: Line intensities from the experiment (circles) and scaled *ab initio* model (PQ/RQ solid line and PP/RR dashed line). Bottom panel: Relative residuals between the experiment and scaled *ab initio* model with error bars equal to the combined standard uncertainty in the measurements.

minimize confounding complications occurring at higher pressure. Importantly, these results can be used to constrain the line intensities in studies involving elevated pressure conditions. Also, the FS-CRDS line intensity measurements [68,80,81] (upon which the HITRAN editions 2008–2020 [40,73–75] were based) were susceptible to non-ideal behavior of the digitizers used to record ring-down decay signals –an effect that was unknown at the time and has been shown to bias measured line intensities [86]. This bias was mitigated in the new FARS-CRDS measurements [64] by using two metrology-grade digitizers.

In addition to potential sources of bias, the new measurements also aimed to minimize and accurately quantify all systematic and statistical sources of uncertainty. Uncertainty in the molecular number density, which depends on pressure, temperature, sample composition, and path-length (for non-CRDS measurements) leads to uncertainty in the line intensity. In previous measurements that contributed to HITRAN updates, where reported, the relative pressure uncertainties spanned from 0.01%–1% [6,68,76,77,80,82], sample composition uncertainties spanned from 0.002%–0.043% [68,76,80,81], and the path-length uncertainties spanned from 0.1%–0.2% [6,82]. The low pressures of the recent measurements by Adkins et al. [64] enabled the use of pure O_2 samples, which minimized the sampling uncertainty. Additionally, a secondary transfer pressure standard directly traceable to NIST primary pressure standards was used to calibrate the pressure gauge of the spectrometer. This metrology-grade approach eliminated the need to rely on the manufacturer's stated uncertainty estimate. The right panel of Fig. 7 depicts how band intensity has changed relative to HITRAN2024 [17] for the past several HITRAN updates. Comparison of the plotted uncertainties highlights the decrease in reported uncertainty in these recent updates. However, the reported values may or may not be based on a complete uncertainty evaluation, which has become increasingly important in data analysis to account for systematic contributions. Uncertainties in the intensities reported by Adkins et al. [64] were based on combining statistical and systematic contributions, which were propagated into the reported scaled *ab initio* model.

In addition to improved measurements, there have been advances in modeling the J-dependence of line intensities in the O_2 A-band. For HITRAN versions 1996–2008 [70–73], the Watson model [66] was used to model the measured intensities. This model, outlined in Gamache et al. [79], includes Hönl-London (HL) factors that capture the non-Boltzmann, rotational dependence of the intensities, and the electron spin coupling to the ground state. In this model [66], the relative line intensities are fixed, where the band intensity is scaled to best fit the experimental data. As the measurement precision improved, a rotational dependence was noted between the Watson model and measured line intensities [68,87,88], leading to the Herman-Wallis-modified Watson (HWW) model being adopted for modeling line intensities from HITRAN versions 2012–2020 [40,74,75]. The Herman-Wallis (HW) modification [67] only empirically accounts for observed deviations from the Watson model [66], because the HW modification was originally derived [89] to treat vibration–rotation effects, while the O_2 A-band comprises rotational-electronic transitions. In contrast to the Watson model, the HWW model adjusts the absolute band intensity and relative band intensities through m-dependent HW coefficients that can be determined through fits to the experimental data.

The scaled *ab initio* model used in Adkins et al. [64] to model the line intensities has several potential advantages over the Watson and HWW band intensity models. First, the *ab initio* intensities are obtained from first principles and therefore can account for physical effects that are not included in the Watson model, and which are only treated empirically by fitting the HWW model to the measured intensities. Second, the empirical nature of the HWW analysis makes it possible to fit measurement biases or collisional effects by introducing additional degrees of freedom. Third, modeling the measured intensities through a sole scaling factor in the *PQ*- and *RQ*-subbranches results in a constant uncertainty contribution from the scaled model in these subbranches, whereas the linear correction term to the *PP*- and *RR*-subbranches exhibits a slight m-dependence in its uncertainty. The functional form of the HW modification means that the uncertainty will always increase with m and will be more significant as additional higher-order terms are included. Finally, with future refinements to *ab initio* calculations that are expected to improve the agreement with the *RR*- and *PP*-subbranches (negating the need for the linear correction), new observations could focus on a limited number of transitions that are optimized for measurement accuracy, while band intensity measurements could be obtained from extrapolation of the *ab initio* calculations to include all relevant transitions.

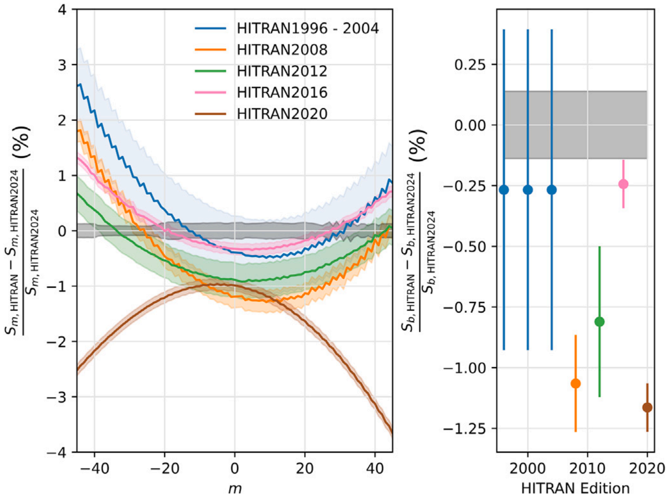

Fig. 7. Comparison of O_2 A-band line intensities, transition dependencies (left panel) and band intensities (right panel), between HITRAN editions 1996–2020 [40,70–75] relative to the scaled *ab initio* intensities included in HITRAN2024 [17]. The shaded regions and error bars represent the uncertainties in the reported band intensity models, where the grey shaded regions indicate the HITRAN2024 uncertainties.

Figure 7 compares the transition-dependent intensities (left panel) and the band intensities (right panel) from the various HITRAN versions [70–73] to the *ab initio* scaled intensity model line intensities [64] included in HITRAN 2024 [17]. Because HITRAN versions 1996–2008 [70–72] used the Watson model, their intensities relative to each other only reflect changes in band intensity. Comparison of the intensities of these earlier HITRAN versions with those of HITRAN2024 [17], reveals an alternating structure between *PP*- and *PQ*-subbranch or *RR*- and *RQ*-subbranch transitions having the same rotational angular momentum quantum number. This result is a manifestation of missing physics in the Watson model associated with differences in the total angular momentum quantum number (see discussion regarding Eqs. (2) and (3)). This behavior is dampened in HITRAN versions 2012–2020, which used the HWW model to model the measured intensities. The addition of the HW factor brought the HITRAN2012 and HITRAN2016 relative intensities into closer agreement with the scaled *ab initio* theoretical intensities, but the relative intensities were still larger than the *ab initio* values at high J. Upon subsequent adjustment of the HW factors in the HITRAN2020 update, the relative intensities were reduced by up to the 4% level at high J. This change caused the relative intensities at high J to be lower than the *ab initio* results.

All band intensities in the previous HITRAN O_2 A-band line lists are smaller than that in HITRAN2024 [17], although the latter intensity is within the uncertainty of the HITRAN1996 – HITRAN2004 values [70–72]. We ascribe the relatively low band intensities for HITRAN2008 – HITRAN2020 [40,73–75] to a combination of unknown biases in these prior measurements and to complications in earlier measurements involving spectra acquired at elevated pressures.

2.5. Oxygen B-band: $b^1\Sigma_g^+(1) \leftarrow X^3\Sigma_g^-(0)$

The last major HITRAN update to the O_2 B-band line list occurred in 2016 [75] when the measured line intensities [90] and SDV line-shape parameters for self-broadened transitions reported in Refs. [90–92] were incorporated into the database. The line positions were based on molecular constants derived by Yu et al. [18]. The Voigt air-broadening line-shape parameters were last updated in HITRAN2012 [74] based on Gordon et al. [93]. The magnitude of the collisional broadening was derived from measurements with limited accuracy and a limited number of studied transitions, while the J-dependence was taken from the O_2 A-band. The collisional shift coefficients were taken from the available measurements or scaled from the A-band when experimental data were unavailable. The HITRAN2024 B-band line list updates the line centers, air-broadening line-shape parameters for Voigt and advanced line profiles, and the advanced line profile line list for self-broadening parameters for select transitions.

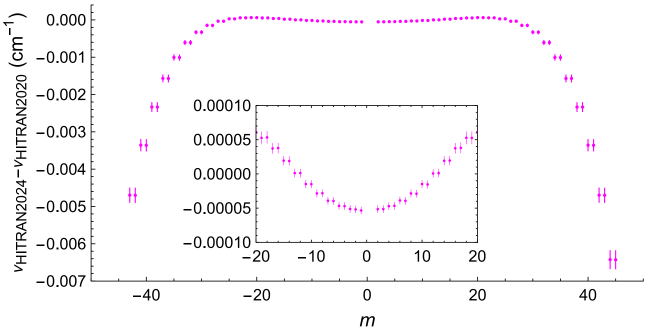

Fig. 8. Comparison between HITRAN2024 line positions in the B-band obtained from the Dunham fit shown in Ref. [94] (Fit #2 in Table 2) and those available in HITRAN2020. The inset shows a zoomed view of the differences for low $|m|$ values. The error bars indicate the standard uncertainty of the Dunham-fit-based line positions from Ref. [94].

2.5.1. Line positions

Line positions for the O_2 B-band are updated in HITRAN2024 [17] to values calculated using spectroscopic constants for the upper state, $b^1\Sigma_g^+(1)$, which were derived by Domysławska et al. [94] from measured line positions (see Fit #2 in Table 2 of Ref. [94]), whereas for the lower state, $X^3\Sigma_g^-(0)$, constants were constrained to those obtained by Yu et al. [18]. The Dunham fit in Ref. [94] included nearly 60 unperturbed transition frequencies (P-branch: $J'' \leq 21$, R-branch: $J'' \leq 38$) measured with CRDS linked to an OFC [90,94]. The spectroscopic constants for the lower state, reported in Ref. [18], are from the Dunham fit based on hundreds of transitions sharing the same lower state, ranging from the microwave to the ultraviolet region. Compared to the previous line positions archived in HITRAN2020 [40], the difference is especially significant for $J'' > 30$, such that for $|m| = 40$ it exceeds 0.003 cm^{-1}. See Fig. 8 for a detailed comparison.

2.5.2. Line-shape parameters: self-perturbed O_2

In the R-branch, non-Voigt line-shape parameters are added to HITRAN2024 [17] for high J transitions ($27 \leq J'' \leq 38$, excluding $J'' = 37$) [94], determined using the SDNG profile. Another seven transitions have upgraded parameters as follows. For two overlapping line pairs, namely R19R19 + R21R21 and R19Q20 + R21Q22, line-mixing [26,95,96] was observed by Domysławska et al. [97] and modeled using first-order theory. For these four lines and three lines from the P-branch, namely P1P1, P7P7, and P9P9, line-shape parameters are also upgraded to the SDNG line profile, because Dicke narrowing was observed for these lines [97,98].

2.5.3. Line-shape parameters: air-perturbed O_2

Air-perturbed line-shape parameters are the subject of the main update to the O_2 B-band transitions for HITRAN2024 [17]. Over 20 transitions from the P- and R-branches have been measured by Bielska et al. [99] with the OFC-referenced FS-CRDS technique at three temperatures (288 K, 296 K, and 328 K). The measurements were performed using a synthetic air sample with 21.04(7)% O_2 in a balance of N_2. These spectra were fit with the SDNG profile, which also enabled the determination of the temperature dependence of the collisional broadening and shift coefficients. The determined temperature dependence of the collisional broadening is the same as for the A-band within the measurement uncertainty [99]. Thus, the A-band collisional broadening temperature dependence replaces the default HITRAN value of 0.71

for the B-band. Previously, HITRAN did not report the temperature dependence of the collisional shift for the O_2 B-band lines; this is now included for HITRAN2024.

For the transitions not investigated in Ref. [99], we approximated the m-dependence of the line-shape parameters with the functions described below (summarized in Table 5). In each case, the functions were used to interpolate parameter values for the unmeasured lines within the m range covered by the measurements, i.e., from $m = -18$ to $m = 14$, for inclusion in the HITRAN2024 database [17]. Parameters for the lines beyond the measurement m range are extrapolated in a parameter-dependent manner as outlined below and indicated in Table 5. In the fitting procedure, we treat line-shape parameter values for different lines labeled by m as being statistically independent. In most cases, the systematic component dominates the experimental uncertainty. The uncertainty in the interpolated line-shape parameter values is the quadrature sum of the correlated error propagation of the interpolation function [100] and the systematic uncertainty. Because extrapolated parameter uncertainties cannot be reliably estimated, they are set to the highest HITRAN uncertainty range (≥20%). Figs. 9 and 10 show the higher-order air-broadening line-shape parameters included for the B-band in HITRAN2024.

The collisional broadening coefficient, $\gamma_{0,\mathrm{air}}$, is approximated by an empirical function previously used for the A-band [101]. In contrast to earlier works [68], we noticed a difference between the collisional broadening coefficients in the P- and R-branches. As a result, different sets of function parameters are fitted for both branches. For the independent variable, instead of J'', we used m :

$$f_{\gamma_{0,\mathrm{air}}}(m) = a_\gamma + \frac{b_\gamma}{1 + c_{\gamma,1}\,|m| + c_{\gamma,2}m^2 + c_{\gamma,4}m^4}\,. \tag{4}$$

Based on the comparison between the B- and A-bands [99], extrapolation to higher $|m|$ lines is done by multiplying the HITRAN2024 A-band $\gamma_{0,\mathrm{air}}$ values by 1.0117(14) [6,17]. The values included in HITRAN2024 from the combination of measurements reported in Ref. [99], the interpolated values, and the scaled A-band values are all shown in Fig. 9. Similarly, the B-band Voigt profile collisional broadening parameter values in HITRAN2024 are scaled from the A-band values using the same multiplicative factor.

The collisional shift coefficient, $\delta_{0,\mathrm{air}}$, is interpolated for unmeasured lines with a model similar to the empirical form proposed for CO_2 by Hartmann [63], which is derived for multiple vibrational bands. Here, it is simplified to the following form:

$$f_{\delta_{0,\mathrm{air}}}(m) = \delta^V_{0,\mathrm{air}}(m) - \Delta N\,\delta^R_{0,\mathrm{air}}(m)\,, \tag{5}$$

where ΔN replaces ΔJ in the original model because $\Delta J = 0$ for the PQ- and RQ-subbranches. $\delta^R_{0,\mathrm{air}}$ and $\delta^V_{0,\mathrm{air}}$ are five-parameter functions that originally were related to the rotational and vibrational contributions to $\delta_{0,\mathrm{air}}$:

$$\delta^R_{0,\mathrm{air}}(m) = a^R_{\delta,1} + a^R_{\delta,2}e^{-|m|b^R_{\delta,1}} + a^R_{\delta,3}e^{-|m|b^R_{\delta,2}}\,, \tag{6}$$

$$\delta^V_{0,\mathrm{air}}(m) = a^V_{\delta,1} + a^V_{\delta,2}e^{-|m|b^V_{\delta,1}} + a^V_{\delta,3}e^{-|m|b^V_{\delta,2}}\,. \tag{7}$$

In this application, data for only the B-band is included. To reduce numerical correlations between parameters, the $a^R_{\delta,3}$ and $b^R_{\delta,2}$ terms were constrained to zero. Extrapolation to higher $|m|$ lines is again based on comparison between the B- and A-bands [99]. Here, the R-branch extrapolated values are obtained by multiplying the HITRAN2024 A-band $\delta_{0,\mathrm{air}}$ values [6,17] by the factor of 1.566(13) obtained from comparison of the collisional shifts for these bands for $m > 8$. In the P-branch, the analogous scaling factor is 1.444(11). To update the Voigt profile collisional shifts, the A-band Voigt values were multiplied by these scaling coefficients for the R- and P-branches. The HITRAN2024 values from measurements, interpolation, and scaling are shown in Fig. 10.

Instead of modeling the speed-dependent collisional broadening coefficient, $\gamma_{2,\mathrm{air}}$, and speed-dependent collisional shift coefficient, $\delta_{2,\mathrm{air}}$, we model the dimensionless speed-dependent parameters $a_{w,\mathrm{air}}$ and $a_{s,\mathrm{air}}$, as defined in Table 1. To interpolate their values for the unmeasured lines, we use the following exponential dependence:

$$f_a(m) = a_{f,1} + a_{f,2}e^{-b_f|m|}\,. \tag{8}$$

In the case of $a_{w,\mathrm{air}}$, we noticed a significant difference between the m-dependencies in the P- and R-branches. Thus, we determined a separate set of parameters for each branch. Extrapolation to higher $|m|$ lines is done using the determined interpolation function for each branch. While $a_{s,\mathrm{air}}$ used the same interpolation function as $a_{w,\mathrm{air}}$, subbranch differences in the measured values indicated each subbranch (*PP, PQ, RR,* and *RQ*) be modeled separately, with the PQ-subbranch constrained to 0. Extrapolation to higher $|m|$ lines is done using the determined interpolation function for each subbranch. Measured, interpolated, and extrapolated values of $a_{w,\mathrm{air}}$ and $a_{s,\mathrm{air}}$ are shown in Figs. 9 and 10, respectively.

The m-dependence of $\tilde{\nu}_{opt}$ was modeled with a third-order polynomial with subbranch-dependent coefficients. The RR- and RQ-subbranches are modeled with the same coefficients. The extrapolation for higher $|m|$ lines is done using mean values calculated for $|m| > 8$ for each subbranch, again the RR- and RQ -subbranches are treated the same.

The temperature dependence of the collisional broadening is determined according to a single power law, as presently done in the HITRAN database and outlined in Table 1. In contrast to other line-shape parameters, no clear m-dependence is observed for this parameter. It is likely that it would be observed if more precise experimental data were available. Based on the comparison reported in Bielska et al. [99] with more accurate A-band results, we adopt the HITRAN2024 A-band parameters for $n_{\gamma_0,\mathrm{air}}$ [6,17] in the B-band for HITRAN 2024. Bielska et al. constrained $n_{\gamma_0,\mathrm{air}} = n_{\gamma_2,\mathrm{air}}$ based on the assumption that $a_{w,\mathrm{air}}$ is temperature-independent [99], which is the constraint used for both the O_2 A- and B-bands in HITRAN2024. B-band measurements did not exhibit a temperature dependence in the $\tilde{\nu}_{opt}$, such that $n_{\nu_{opt}}$ is 0 [99]. The outlook section of this work includes a related discussion about the different constraints used in higher-order parameter temperature dependencies in the O_2 B-, A-, and 1.27 μm bands included in HITRAN2024.

We account for the temperature dependence of the collisional shift coefficient, $\delta'_{0,\mathrm{air}}$, according to the linear model, as shown in Table 1. For the available data, its m-dependence can be modeled according to the Eq. (8). However, separate sets of coefficients are required for the P- and R-branches. Similarly to the case of the speed-dependence parameters, the extrapolation to higher $|m|$ lines is done using the interpolation functions. The $a_{s,\mathrm{air}}$ measurements did not exhibit a temperature dependence [99].

2.6. Schumann-Runge bands: $B^3\Sigma_u^-(v) \leftarrow X^3\Sigma_g^-(v)$

The Schumann–Runge (SR) bands are a complex system of thousands of predissociative absorption lines between ∼175 nm and ∼205 nm. Photodissociation in the SR region is a significant source of atomic oxygen and ozone in the stratosphere and mesosphere [102], while photoabsorption by O_2 in the SR bands also controls the depth of penetration of solar vacuum ultraviolet (VUV) radiation into the atmosphere and consequently indirectly determines the photodissociation rates of other atmospheric species. In atmospheric applications, the SR bands are normally modeled using the line-by-line (LBL) technique, in which a synthetic spectrum is constructed by adding together contributions from individual rovibronic lines, which are described by Voigt profiles [103].

From HITRAN1996 [70] onward, the line positions, intensities, and predissociation linewidths used in the SR LBL algorithm reported by Minschwaner et al. [104], based on work by Yoshino et al. [105], Veseth and Lofthus [106], Lewis et al. [107,108], Tatum and Watson [109], and Cheung et al. [110,111], have been included in HITRAN.

Table 5
Outline of the empirical functions and parameters modeling air broadening line-shape parameters for the O_2 B-band. The branch column not only indicates the applicable branch for the given parameters, but the label in parentheses indicates whether the parameters in a row are applied to all reported B-band transitions in HITRAN2024 (all), the interpolated transitions (int. - unmeasured transitions between m = [−18, 14]), or the extrapolated transitions (ext. - transitions outside of measured range = [−18, 14]). Uncertainties in parameters are provided in the supplementary materials.

	Branch	$a_\gamma + \frac{b_\gamma}{1+c_{\gamma,1}\lvert m\rvert+c_{\gamma,2}m^2+c_{\gamma,4}m^4}$ a_γ	b_γ	$c_{\gamma,1}$	$c_{\gamma,2}$	$c_{\gamma,4}$
$\gamma_{0,\text{air}}$ (cm^{-1} atm^{-1})	P (int.)	0.02844	0.03461	0.08863	−0.003258	7.129×10^{-6}
	R (int.)	0.03965	0.03625	0.3501	−0.01255	5.138×10^{-5}
	P & *R* (ext.)	1.01173 $\gamma_{0,\text{air}}^{A-band}$	0	0	0	0
$n_{\gamma_{0,\text{air}}}$	All	$n_{\gamma_{0,\text{air}}}^{\text{A-band}}$				
$\delta_{0,\text{air}}$ (cm^{-1} atm^{-1})	Branch	$\delta_{0,\text{air}}^V(m) - \Delta N \delta_{0,\text{air}}^R(m)$ $\delta_{0,\text{air}}^R(m) = a_{\delta,1}^R + a_{\delta,2}^R e^{-\lvert m\rvert b_{\delta,1}^R} + a_{\delta,3}^R e^{-\lvert m\rvert b_{\delta,2}^R}$ $\delta_{0,\text{air}}^V(m) = a_{\delta,1}^V + a_{\delta,2}^V e^{-\lvert m\rvert b_{\delta,1}^V} + a_{\delta,3}^V e^{-\lvert m\rvert b_{\delta,2}^V}$ $a_{\delta,1}^R$	$a_{\delta,2}^R$	$b_{\delta,1}^R$	$a_{\delta,3}^R$	$b_{\delta,2}^R$
	P & *R* (int.)	0.0016014	−0.0030266	0.031542	0	0
		$a_{\delta,1}^V$	$a_{\delta,2}^V$	$b_{\delta,1}^V$	$a_{\delta,3}^V$	$b_{\delta,2}^V$
	P & *R* (int.)	−0.10143	0.0064244	0.57552	0.094056	0.0017639
		Scaled A-band				
	P (ext.)	1.44423 $\delta_{0,\text{air}}^{\text{A-band}}$				
	R (ext.)	1.56602$\delta_{0,\text{air}}^{\text{A-band}}$				
	Branch/Subbranch	$a_{f,1} + a_{f,2}e^{-b_f\lvert m\rvert}$ $a_{f,1}$		$a_{f,2}$		b_f
$\delta'_{0,\text{air}}$ (cm^{-1} atm^{-1} K^{-1})	*P* (int. & ext.)	2.819×10^{-5}		-2.478×10^{-5}		0.4050
	R (int. & ext.)	2.822×10^{-5}		-2.779×10^{-5}		0.1930
$a_{w,\text{air}}$	*P* (int. & ext.)	0.1189		−0.05605		0.04160
	R (int. & ext.)	0.08353		−0.06186		0.3927
$a_{s,\text{air}}$	*PP* (int. & ext.)	−0.04116		1.069		1.761
	PQ (int. & ext.)	0		0		0
	RR (int. & ext.)	−0.03211		0.5205		0.5001
	RQ (int. & ext.)	−0.004281		0.2301		0.2999
	Branch/Subbranch	$a_{v,0} + a_{v,1}\lvert m\rvert + a_{v,2}\lvert m\rvert^2 + a_{v,3}\lvert m\rvert^3$ $a_{v,0}$		$a_{v,1}$	$a_{v,2}$	$a_{v,3}$
$\tilde{\nu}_{opt,\text{air}}$ (cm^{-1} atm^{-1})	PP (int.)	0.004657		−0.0008481	8.190×10^{-5}	-2.356×10^{-6}
	PQ (int.)	0.003048		−0.0004184	3.618×10^{-5}	-8.791×10^{-7}
	R (int.)	0.007142		−0.001685	0.0001797	-6.053×10^{-6}
	All (ext)	subbranch/branch avg. meas. |m| > 8				
$n_{\gamma_{2,\text{air}}}$	All	$n_{\gamma_{0,\text{air}}}^{A-band}$				
$\delta'_{2,\text{air}}$ (cm^{-1} atm^{-1} K^{-1})	All	$\delta'_{0,\text{air}} \frac{\delta_{2,\text{air}}(T_r)}{\delta_{0,\text{air}}(T_r)}$				
$n_{\nu_{opt,\text{air}}}$	All	0				

Fig. 11 highlights changes to the HITRAN editions from 2000 to the present in the spectral region of the SR bands, identifying two key inconsistencies introduced in HITRAN2008 [73] and HITRAN2016 [75], which have been remedied in HITRAN2024 [17].

The HITRAN2008 [73] edition introduced changes in the data for the SR bands, including the recalculation of associated parameters such as Einstein A-coefficients ($A_{i,j}$) and statistical weights. Additionally, HITRAN2008 reported the predissociation linewidths as half width at half maximum (HWHM) values, whereas earlier editions used full width at half maximum (FWHM) [73]. A recent study by Ji et al. [112], noted an apparent discrepancy between HITRAN2020 [40] and HITRAN2000 [71] linewidths in the SR bands, when computing low-resolution correlated *k*-coefficients in 1-D models. Tomazzeli et al. [113] compared the predissociation linewidths reported in HITRAN2000 [71] and HITRAN2020 [40] with those reported by Cheung et al. [110] confirming that the linewidths in HITRAN2020 are half as large as those reported by Cheung et al. [110] and HITRAN2000 [71]. A detailed analysis of HITRAN versions from 2000 onward revealed that this error was introduced in the 2008 edition when the database was reformatted to convert the linewidths to HWHM, with this error being propagated to subsequent HITRAN editions. HITRAN2024 has corrected this inconsistency by multiplying HITRAN2020 predissociation linewidths by 2.

Prior to HITRAN2016, the entries for the SR bands were provided separately from the rest of the HITRAN database. Beginning in HITRAN2016, this data has been included in the HITRAN LBL format in HITRANonline [21,75]. Tomazzeli et al. [113] found that HITRAN2020 includes default values equal to 0.04 for $\gamma_{0,\text{air}}$ and $n_{\gamma_{0,\text{air}}}$ for all transitions in the SR bands. These values are not valid for predissociative lines, which are not pressure dependent. It should be noted that neither HITRAN2016 [75] nor HITRAN2020 [40] mentions introducing nonzero default values to $\gamma_{0,\text{air}}$ and $n_{\gamma_{0,\text{air}}}$ in the SR bands. To remedy this error, HITRAN2024 has provided a Python script to appropriately use HITRAN2024 LBL data for predissociative transitions in the SR bands.

2.7. Broadening by CO_2

In order to accommodate the modeling of radiative transfer in planetary atmospheres, it is important to account for the broadening of lines by ambient gases that dominate these atmospheres. To that end, for line lists of many molecules, HITRAN now includes line-shape parameters associated with broadening of H_2, He, CO_2 [114], and H_2O [115]. For the lines of oxygen, only broadening by water vapor was introduced in HITRAN2020 [40,115]. In this edition, broadening by carbon dioxide has also been added, based on the work by Petrova et al. [116]. In that work, CO_2-broadening parameters were measured in the A-band. It was found that the ratio of $\gamma_{0,\text{CO2}}/\gamma_{0,\text{air}}$ in the A-band does

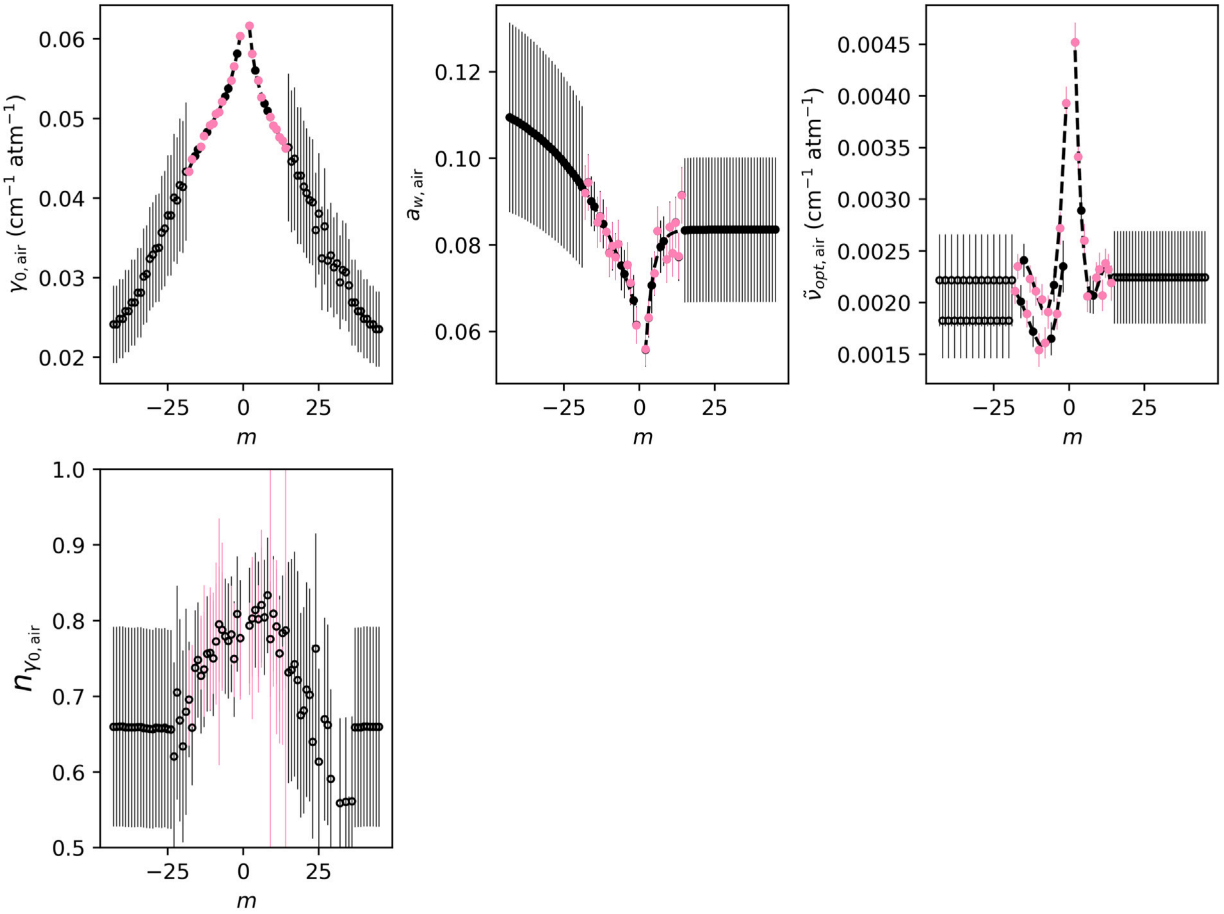

Fig. 9. Air-perturbed pressure broadening and temperature dependence, speed-dependent broadening, and Dicke narrowing parameters versus total angular momentum index for the B-band. The dashed lines are the empirical models given by Eqs. (4), (8) with coefficients from Table 5. The symbols represent values included in HITRAN2024, where the colored points show experimental values reported in Ref. [99], the black solid points are the non-measured transitions determined from the empirical model, and the black open points are the non-measured transitions determined from scaled A-band or fixed values. The standard uncertainties are shown with error bars with magnitudes for measured transitions from Ref. [99] and for interpolated transitions from correlated error propagation. Values extrapolated beyond the range of measured values have uncertainties of 20%. The collisional broadening temperature dependence was fixed to the A-band values; here, the colored error bars indicate the uncertainties reported for the measured transitions.

not exhibit noticeable rotational dependence and is basically a constant of 1.18. Interestingly, it coincides precisely with the ratio obtained in the pure rotational band by Golubiatnikov et al. [117]. Therefore, in order to provide γ_{0,CO_2} for all lines of oxygen in HITRAN, for all bands of all isotopologues, the Voigt half-widths ($\gamma_{0,\mathrm{air}}$) have been multiplied by 1.18.

2.8. Collision-induced absorption

In the terrestrial atmosphere, collision-induced absorption (CIA) by O_2–O_2 and O_2–N_2 collisional pairs results in prominent spectral features throughout many wavelengths. In fact, in the UV the O_2–O_2 CIA spectra correspond to the dominant oxygen-related absorption. The extensive update of O_2–O_2 and O_2–N_2 CIA at different wavelengths is not addressed in this paper, but is described in a manuscript devoted to the global update of the CIA in HITRAN [118].

3. Recommendations and outlook for HITRAN2024 and beyond in oxygen spectroscopy

In the previous section, we outlined the O_2 updates to the HITRAN2024 database. In the next section, we discuss recommendations and outlook for O_2 spectroscopy beyond the HITRAN2024 edition [17].

3.1. Definition of air in O_2 line-shape parameters

The HITRAN database traditionally provides self- and air-broadened line-shape parameters. However, because the absorbing molecule in the present case is a major component of air, this is a rare situation where collisional broadening by self (O_2–O_2) and foreign (O_2–N_2) partners are the principal contributions to the line-shape. Because experimental relative uncertainties in $\gamma_{0,\mathrm{O2}}$ now approach the part-per-thousand level, biases introduced by inconsistent definitions of air, in both the amount fraction of O_2 and the inclusion of other less-abundant components of air, become evident when comparing literature values. Therefore, the choice of a more precise and standardized definition of the composition of air becomes important in the uncertainty quantification of line-shape parameters. Recent studies in the O_2 A- [119] and 1.27 μm bands [61] highlighted some of these issues.

In a recent study of the O_2 A-band, the average ratio of collisional broadening by N_2 to O_2 was reported to be $\langle \gamma_{0,\mathrm{N2}}/\gamma_{0,\mathrm{O2}} \rangle = 0.94 \pm 0.07$ [119], where the carets indicate an average and standard deviation of all transitions up to $J = 40$. Consequently, small differences from a nominal O_2 amount fraction of 0.21 can cause error in $\gamma_{0,\mathrm{air}}$, while this bias grows with increasing departure from the nominal O_2 amount fraction in air [61]. For example, using the $\gamma_{0,\mathrm{N2}}$ and $\gamma_{0,\mathrm{O2}}$ values from Stevenson et al. [119] a sample with an O_2 amount fraction of 0.2 would result in a $\gamma_{0,\mathrm{air}}$ value −0.27% to 0.01% different than a sample with an O_2 amount fraction of 0.21, depending on the transition. A second point addressed in both studies was the impact of neglecting

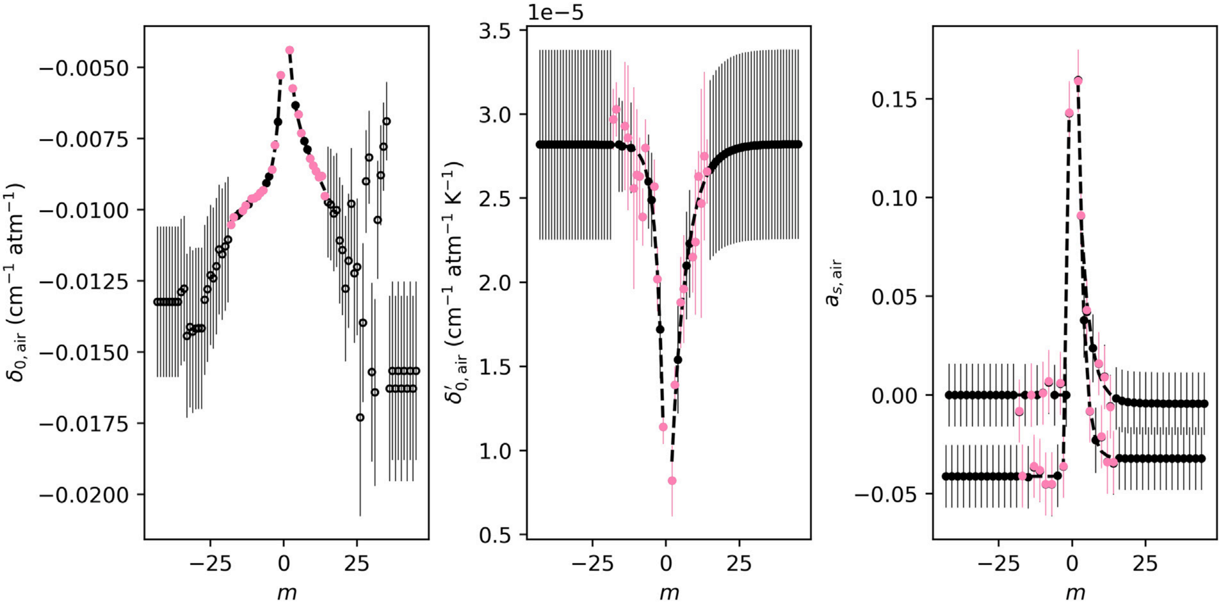

Fig. 10. Air-perturbed collisional shifting and temperature dependence, and speed-dependent shifting parameters versus total angular momentum index for the B-band. The dashed lines are the empirical models given by Eqs. (5), (6), (7), (8) with coefficients from Table 5. The symbols represent values included in HITRAN2024, where the colored points are measured values reported in Ref. [99], the solid black points are the non-measured values determined by the empirical model, and the open black points are from A-band scaled or fixed values. The standard uncertainties are shown with error bars with magnitudes for measured transitions from Ref. [99] and for interpolated transitions from correlated error propagation. Extrapolated transition uncertainties are fixed to 20%.

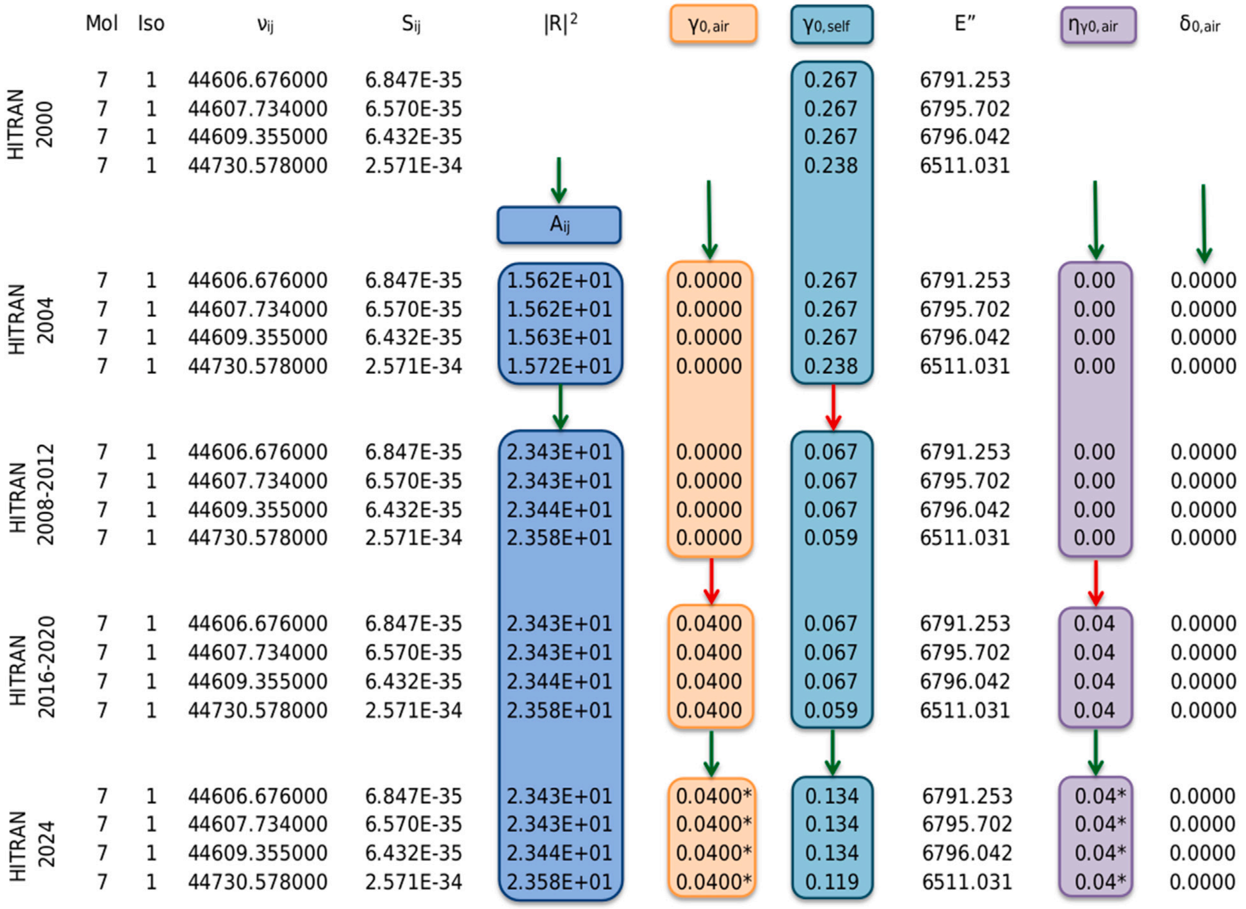

	Mol	Iso	ν_{ij}	S_{ij}	$\|R\|^2$	$\gamma_{0,\mathrm{air}}$	$\gamma_{0,\mathrm{self}}$	E″	$\eta_{\gamma0,\mathrm{air}}$	$\delta_{0,\mathrm{air}}$
HITRAN 2000	7	1	44606.676000	6.847E-35			0.267	6791.253		
	7	1	44607.734000	6.570E-35			0.267	6795.702		
	7	1	44609.355000	6.432E-35			0.267	6796.042		
	7	1	44730.578000	2.571E-34			0.238	6511.031		
					A_{ij}					
HITRAN 2004	7	1	44606.676000	6.847E-35	1.562E+01	0.0000	0.267	6791.253	0.00	0.0000
	7	1	44607.734000	6.570E-35	1.562E+01	0.0000	0.267	6795.702	0.00	0.0000
	7	1	44609.355000	6.432E-35	1.563E+01	0.0000	0.267	6796.042	0.00	0.0000
	7	1	44730.578000	2.571E-34	1.572E+01	0.0000	0.238	6511.031	0.00	0.0000
HITRAN 2008-2012	7	1	44606.676000	6.847E-35	2.343E+01	0.0000	0.067	6791.253	0.00	0.0000
	7	1	44607.734000	6.570E-35	2.343E+01	0.0000	0.067	6795.702	0.00	0.0000
	7	1	44609.355000	6.432E-35	2.344E+01	0.0000	0.067	6796.042	0.00	0.0000
	7	1	44730.578000	2.571E-34	2.358E+01	0.0000	0.059	6511.031	0.00	0.0000
HITRAN 2016-2020	7	1	44606.676000	6.847E-35	2.343E+01	0.0400	0.067	6791.253	0.04	0.0000
	7	1	44607.734000	6.570E-35	2.343E+01	0.0400	0.067	6795.702	0.04	0.0000
	7	1	44609.355000	6.432E-35	2.344E+01	0.0400	0.067	6796.042	0.04	0.0000
	7	1	44730.578000	2.571E-34	2.358E+01	0.0400	0.059	6511.031	0.04	0.0000
HITRAN 2024	7	1	44606.676000	6.847E-35	2.343E+01	0.0400*	0.134	6791.253	0.04*	0.0000
	7	1	44607.734000	6.570E-35	2.343E+01	0.0400*	0.134	6795.702	0.04*	0.0000
	7	1	44609.355000	6.432E-35	2.344E+01	0.0400*	0.134	6796.042	0.04*	0.0000
	7	1	44730.578000	2.571E-34	2.358E+01	0.0400*	0.119	6511.031	0.04*	0.0000

Fig. 11. Extract of the HITRAN database versions from 2000 [71], 2004 [72], 2008–2012 [73,74], 2016–2020 [40,75], and 2024 [17]. Where Mol is the molecular species identification (ID) number, Iso is the isotopologue ID number $\nu_{i,j}$ is the wavenumber of the spectral line transition in vacuum (cm^{-1}), $S_{i,j}$ is the spectral line intensity (cm^{-1} molec.$^{-1}$ cm^2), $|R|^2$ is the weighted square of the transition moment (D^2), A_{ij} is the Einstein-A coefficient of the transition (s^{-1}), and E'' is the lower-state energy of the transition (cm^{-1}). Green arrows indicate updates, and red arrows indicate inadvertent errors.

Ar-broadening contributions to air-broadening parameters. The ratio $\langle \gamma_{0,\mathrm{Ar}}/\gamma_{0,\mathrm{O2}} \rangle = 0.69 \pm 0.19$ in the O_2 A-band [119] was reported, with similar observed magnitudes in the 1.27 μm band [61]. The inclusion of Ar broadening in $\gamma_{0,\mathrm{air}}$ determined from measurements using synthetic air (only O_2 and N_2), decreased the bias, from 0.33% to 0.17%, between $\gamma_{0,\mathrm{air}}$ determined from whole air (containing Ar) and synthetic air in the 1.27 μm band [61]. In the A-band study by Stevenson et al. [119], simulations and atmospheric observations investigated the impact of neglecting Ar broadening on surface pressure retrievals. These analyses suggested that the effect will be small (0.07%) but non-negligible by comparison to retrieval target precisions. Specifying the definition of air in terms of amount fraction and inclusion of the broadening contribution by Ar in publications can allow for more consistent reporting in reference databases, like HITRAN, and improved uncertainty quantification in the literature.

3.2. Future updates to 60 GHz manifold

The transitions between spin components within different rotational levels cluster around 60 GHz, giving rise to a very strong and broad (±10 GHz) absorption feature. These lines are routinely employed in radiometric atmospheric measurements for the retrieval of temperature distribution [120]. The modeling of this feature is complicated by very strong line mixing due to the very close proximity of lines to each other. To eliminate the uncertainties [121] in the models, this band has been studied extensively in recent years in Nizhny Novgorod [50,122–127]. Not only have individual spectroscopic parameters been measured with unprecedented accuracy (and advanced line shapes), but also the code that calculates full line-mixing has been developed [125]. This code will be updated with the most accurate parameters and included in future editions of the HITRAN database.

3.3. Ab initio line intensities

A previous section describes the update to the line intensities in the O_2 A-band [64] that are being incorporated in the HITRAN2024 update [17], where the O_2 B-band line intensities were last updated in HITRAN2016 [75,90], and the 1.27 μm band line intensities were last updated in HITRAN2020 [40,43]. In the section describing the O_2 A-band line intensity updates, we highlight the historical evolution of models used by HITRAN for this band [64,66,67], where the HITRAN2024 [17] O_2 A-band update uses an *ab initio* scaling approach to model measured line intensities [64,65]. In this section, we explore the current applicability of the scaled *ab initio* approach to modeling the B-, A-, and 1.27 μm bands of O_2. We do this by modeling the HITRAN2024 line intensities [17] for these bands [43,64,79,90] by scaling recently published *ab initio* line intensities [65] to capture measured band intensities. It should be emphasized that this is a forward-looking analysis, and for the O_2 HITRAN2024 update [17] the A-band is the only band that uses the *ab initio* scaling intensity model for the reported line intensities [64].

Figure 12 depicts the results obtained by scaling the *ab initio* intensities [65] by respective multiplicative factors, β, which were determined by least-squares fits to the HITRAN2024 intensities [17,43,64,79,90] for these three bands. The residuals for each O_2 band are displayed in the lower panel. For the A-band, the *PQ*- and *RQ*-subbranches show no systematic residuals because this single-factor scaling of the *ab initio* band intensities to measured values was previously used in the determination of the HITRAN2024 line intensities, whereas the relatively small *PP*- and *RR*-subbranch discrepancy (discussed above) was treated by adding a linear m-dependent scaling term. The HITRAN2024 1.27 μm band line intensities are based on fitting the product of the J-dependent Hönl-London factors and a Herman-Wallis (HW) -like correction to measurements. This approach is analogous to the HWW model previously used in the A-band. In the 1.27 μm band, the HW parameters were determined separately for subbranches with common ΔS values. Like the A-band, the 1.27 μm band shows systematic subbranch-dependent residuals upon scaling the *ab initio* intensities to model the HITRAN2024 values [17]. In this case, three distinct subbranch groupings occur: $\Delta S = -1$ (*QP, RQ, SR*); $\Delta S = 0$ (*PP, QQ, RR*); and $\Delta S = 1$ (*OP, PQ, QR*). The shape of the residuals for each ΔS value is similar to the shape of the HW terms reported in [43].

The O_2 B-band line intensities in HITRAN2024 [17] are from high-resolution CRDS measurements for low- and mid-N transitions (depicted by closed circles in left panels of Fig. 12) [90] and Watson model intensities at higher N (open circles in left panels of Fig. 12) [79]. The transition between the two sources is evident in the residuals, which have better agreement with scaled *ab initio* intensities for the lower N line intensities and diverging behavior at higher N. Unlike the A- and 1.27 μm bands, the B-band residuals show a branch rather than subbranch dependence. Bielska et al. reported line intensities of three lines in the P-branch of the B-band with relative differences from the current HITRAN intensities of 1.5%–3% [98]. These literature differences in measured line intensities motivate additional experimental measurements in the B-band for a broader range of transitions. Additional high-accuracy line intensity measurements in the B-band would also provide confirmation of the ΔN rather than ΔS deviation from the *ab initio* line intensities.

The future adoption of *ab initio* calculations to model O_2 intensities will require challenging refinements of theory to account for the observed branch and subbranch dependencies as well as to predict absolute band intensities. For the A- and 1.27-μm bands, experimental uncertainties are already sufficiently small to provide robust constraints on the observed subbranch variations as well as the integrated band intensities needed to guide advances in theory. Nevertheless, there remain experimental challenges for relatively weak bands such as the B-band, although as can be seen in Fig. 12, there are statistically significant differences in the relative intensities obtained by experiment and *ab initio* theory. Assuming that *ab initio* calculations will eventually predict the observed trends in Fig. 12 as well as band intensities, calculations of this quality will enable confident extrapolation to higher J lines and should be applicable to weaker bands that are currently difficult to measure. With that in mind, it should be noted that the bands involving higher vibrational levels of the $b^1\Sigma^+$ state, namely, the γ and δ bands (corresponding to $v' = [2, 3]$), have not been updated in HITRAN2024 but could benefit from further experimental and theoretical investigations.

3.4. Line-shape parameter comparison across bands

Here we consider predicted and measured J-dependencies of higher-order O_2 line-shape parameters for different bands. Tran et al. [128], carried out requantized classical molecular dynamics simulations (rCMDS) to predict absorption spectra of O_2 in air from which SDNG profile line-shape parameters and their temperature dependencies were retrieved for lines with N'' up to 25. It is worth noting that these simulations cannot predict band-, branch-, or subbranch-dependencies of line-shape parameters because the underlying physical model does not account for the electronic nature of the O_2 transitions. The rCMDS-derived line-shape parameters were compared to those obtained from fits of seven air-broadened O_2 lines of the 1.27 μm band, measured with an FS-CRDS spectrometer [128]. The results showed that the calculated broadening coefficients are, on average, 2% smaller than the measured values, while the fitted higher-order line-shape parameters are in good agreement with the measurements. This result was later confirmed by comparing rCMDS results with other measurements in the 1.27 μm band [46]. In Ref. [128], the predicted values of $\tilde{\nu}_{opt,\mathrm{air}}$ and $\gamma_{2,\mathrm{air}}$ were also used as constant SDNG profile line-shape parameters in the least-squares fit analysis of measured spectra. The results showed that with the use of these predicted parameters, all the measured lines could be fit to within 1% –which was much better than the best fits of the Voigt profile to the measured spectra.

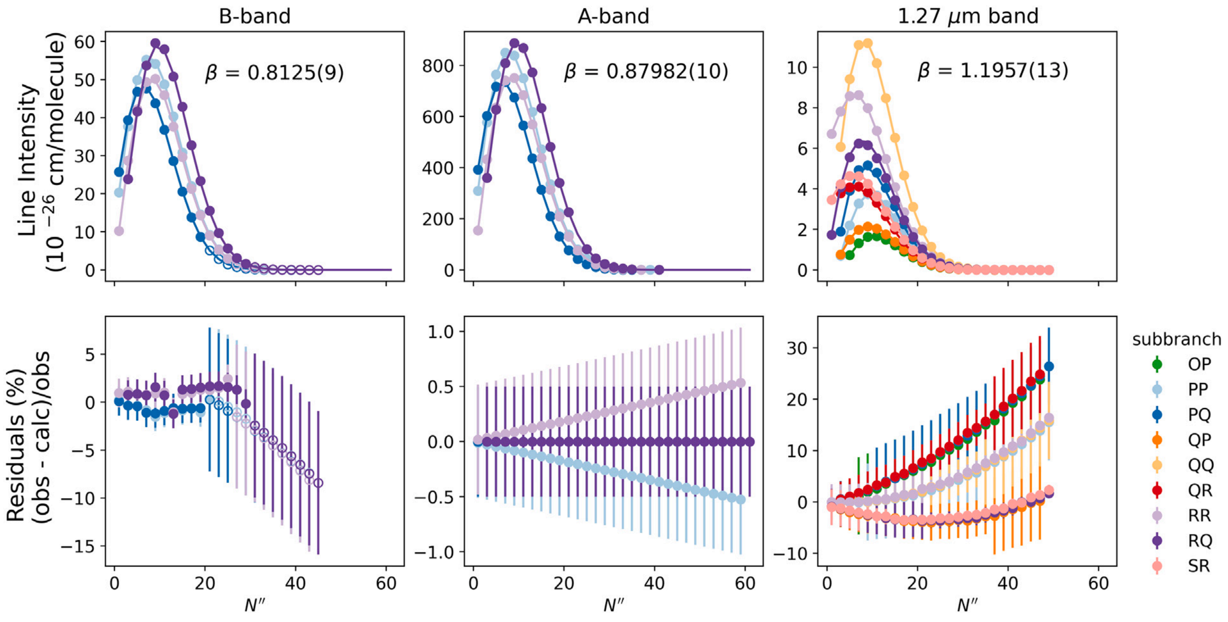

Fig. 12. Model and residuals for *ab initio* intensities scaled by β for the O_2 B [79,90], A [64], and 1.27-μm – [43]-bands. Top panel: Line intensities from HITRAN2024 [17] (circles) and the scaled *ab initio* model [65]. Bottom panel: Relative residuals between HITRAN2024 and scaled *ab initio* model. Relative uncertainties represent the middle range of the HITRAN uncertainty code for a given transition. For a more refined discussion of the A-band uncertainties, see Adkins et al. [64].

To assess the magnitude of band-to-band differences in air-broadened line-shape parameters, we expand the previous analysis by comparing these quantities and their temperature dependencies given in HITRAN2024 for the O_2 B-, A-, and 1.27 μm bands [6,48,61,99] [17] to corresponding rCMDS values. This comparison addresses whether band- and/or branch-dependent differences in HITRAN2024 [17] line-shape parameters, which are not captured by the rCMDS simulations, are important. These comparisons provide insight regarding the appropriateness of using rCMDS-based theoretical constraints when extracting line-shape parameters and temperature exponents from measured spectra. They also reveal the extent to which high-accuracy data in one band might be used to supplement available measurements in another band for use in spectroscopic reference databases like HITRAN.

Figure 13 shows HITRAN-to-rCMDS line parameter ratios for the B-, A-, and 1.27 μm bands corresponding to the following parameters: $\gamma_{0,\mathrm{air}}$, $a_{w,\mathrm{air}}$, $\tilde{\nu}_{opt,\mathrm{air}}$, and $n_{\gamma_{0,\mathrm{air}}}$. The $n_{\gamma_{2,\mathrm{air}}}$ and $n_{\nu_{opt,\mathrm{air}}}$ coefficients are also directly compared in this figure for the O_2 bands as well as the corresponding rCMDS temperature exponents. In the line-shape parameter subplots, we represent two different rCMDS uncertainty metrics. The first is a dark-shaded region representing the 3σ fit uncertainty reported for the rCMDS-derived line-shape parameters. The lighter-shaded region is a sensitivity metric, which was evaluated as the relative difference between the fitted and SDNG profile rCMDS-constrained parameter values reported in Tran et al. [128]. This quantity represents the numerical correlation between a_w and $\tilde{\nu}_{opt}$, such that there is a range of narrowing parameter combinations that minimize spectral residuals.

In general, the HITRAN2024 line-shape parameters and collisional broadening temperature dependencies [17] exhibit less variation between the compared O_2 bands than with the rCMDS-derived line-shape parameters. For the collisional broadening ratio between HITRAN2024 and rCMDS, given by $\gamma_0/\gamma_{0,\mathrm{rCMDS}}$, all three bands exhibit a pronounced asymmetry between the P- and R-branches at low to mid – $|m|$ (<15), with the rCMDS values being larger than the measured γ_0 values by as much as 10% for $|m| \approx 20$.

Nevertheless, there are some statistically significant band-to-band deviations between the HITRAN2024 line-shape parameters of Fig. 13 that can be at least partially attributed to differences in the experimental conditions (e.g., sample composition) and spectral analysis methods (e.g. choice of line profiles and constraints) used for data reduction. For example, the line-shape parameters of the B- and 1.27 μm bands, were derived from SDNG profile fits to air-broadened mixtures. In contrast, the A-band results correspond to SDV profile fits to measured spectra comprising samples that ranged from being mostly N_2-broadened to those that were self-broadened, with the a_w term constrained to be broadener independent [6]. There are band-to-band differences in γ_0 which are most prominent at low-$|m|$, although they are significantly smaller for $|m| > 10$ in the P-branch and $|m| > 15$ in the R-branch. Differences in the a_w values between those of the A-band and the other two bands can also be attributed in part to the abovementioned constraint on this quantity and choice of line profile. This finding highlights the importance of considering the choice of line profiles and constraints imposed when comparing line-shape parameters reported by different studies. To first order, there is sufficient agreement between the B- and 1.27 μm band narrowing parameters ($a_{w,\mathrm{air}}$ and $\tilde{\nu}_{opt,\mathrm{air}}$), such that without higher precision spectroscopic measurements, the parameters in these bands could be considered to be band-independent. Additionally, the HITRAN-to-rCMDS value ratios for $a_{w,\mathrm{air}}$ and $\tilde{\nu}_{opt,\mathrm{air}}$ show W- and M-shaped structure with m, respectively, suggestive of numerical correlation between these values. This effect is further evidenced by the rCMDS sensitivity metric, which captures most of the scatter in the HITRAN-to-CMDS ratios for $a_{w,\mathrm{air}}$ and $\tilde{\nu}_{opt,\mathrm{air}}$. This result suggests that in measurements where these parameters show evidence of numerical correlation, one of the values or the ratio of the parameters could be constrained to the CMDS-derived parameters or another sensible constraint.

Within the measurement uncertainty, the A- and 1.27 μm bands show good agreement for $n_{\gamma_{0,\mathrm{air}}}$ in the P-branch and through mid-m values in the R-branch. However, there is a pronounced M-shaped structure in the HITRAN-to-rCMDS ratio values, with the deviation being most pronounced at higher $|m|$. Because of the good agreement between the A- and 1.27 μm bands, $n_{\gamma_{0,\mathrm{air}}}$ could also be considered as being band-independent. Regarding HITRAN2024 values of $n_{\gamma_{0,\mathrm{air}}}$ in the B-band and as discussed in the updates for this band, the HITRAN2024 A-band $n_{\gamma_{0,\mathrm{air}}}$ values were adopted because measurement uncertainty precluded the determination of the m-dependence of this quantity [99].

In spectral analyses, the higher-order line-shape parameters are often assumed to have various constraints for the temperature dependencies, which should be considered when comparing results. In the O_2 A- and B-bands, it has been assumed that the speed-dependent broadening has the same temperature dependence as the collisional broadening (or equivalently $a_{w,\mathrm{air}}$ is temperature independent), whereas for the 1.27 μm band it was reported that $\gamma_{2,\mathrm{air}}$ had a smaller temperature dependence than $\gamma_{0,\mathrm{air}}$ [61]. The rCMDS-derived temperature dependencies exhibit highly variable temperature exponents for $\gamma_{2,\mathrm{air}}(m)$, likely because of the small signal-to-noise ratio of the rCMDS-calculated spectra (~500), and the fact that the temperature exponents were directly retrieved from fits of the spectra calculated at low temperatures rather than from the line-shape parameters themselves [128]. The 1.27 μm band study [61] determined $n_{\nu_{opt,\mathrm{air}}}$ by averaging over all measured transitions, where the authors reported a temperature exponent of 1.9. The B-band study [99] did not yield a measurable temperature dependence of $\tilde{\nu}_{opt}$. Whereas for the rCMDS calculation of $\tilde{\nu}_{opt}$, a temperature exponent of unity was assumed, consistent with that predicted by molecular diffusion [128].

While rCMDS-derived parameters are not available for the pressure shifting line-shape parameters, $\delta_{0,\mathrm{air}}$ and $\delta_{2,\mathrm{air}}$ we can still compare experimental values between the three visible and NIR O_2 bands of focus here (Fig. 14). We see a roughly factor of five difference in the magnitude of the pressure shifting across these bands, with the B-band having the largest magnitudes and 1.27 μm band the smallest. The linear temperature dependence of $\delta_{0,\mathrm{air}}$ is consistent for the A- and B-bands, but it is substantially lower in magnitude for the 1.27 μm band. The a_s term is highly uncertain and only reported for the B- and 1.27 μm bands. The agreement between these bands is reasonable in the *R*-branch but shows more pronounced differences in the *P*-branch. Further measurements of this quantity, specifically in the A-band, would be necessary to determine if it could be constrained across bands. For measurements of the B- and 1.27 μm bands, the respective fitted speed-dependent shifting terms $a_s = \delta_2/\delta_0$ [99], and δ_2 [61], were reported to be temperature independent. Thus, in the case of the B-band, $\delta_2' = \delta_0' a_s$, whereas for the 1.27 μm band $\delta_2' = 0$.

Comparing the line-shape parameters and temperature exponents between bands and with the corresponding rCMDS-derived values is useful in determining the potential for constraints in analysis and for including these values in spectroscopic reference databases, like HITRAN. Additionally, comparisons of this type highlight the need for the next generation of higher-accuracy measurements and theory. Measured O_2 A-band line-shape parameters obtained with the SDNG profile are needed to provide a consistent comparison with the B- and 1.27 μm band higher-order line-shape parameters. Additionally, theoretical and measured temperature exponents for the higher-order line-shape parameters are needed. These data would indicate whether some or all line-shape parameter temperature exponents could be constrained across various visible and NIR O_2 bands. Finally, because rCMDS theory does not account for observed differences in line-shape parameters between bands, branches, and subbranches, there is ample opportunity for complementary theoretical approaches (e.g., *ab initio*) to provide additional insights.

Indeed, recent methodological advances make it possible to populate the spectroscopic databases with accurate *ab initio* line-shape parameters based on fully quantum calculations, and this prospect has great potential to play an increasingly important role in future editions of HITRAN. For O_2 line-shape parameters, the accuracy reached by fully quantum calculations is evidenced by the first *ab initio* treatment of N_2-induced pressure broadening of the 118 GHz fine structure line [129]. These calculations were in good agreement with measured values over a wide range of temperatures (cf. Fig. 8 in Ref. [129]). Moreover, the theoretical approach allows the explicit determination of the band- and branch-dependence of line-shape parameters, as was demonstrated for He-perturbed spectra of H_2 [130] and HD [131]. One challenge of the *ab initio* methodology is the accurate evaluation of pressure-induced shifts, because the results often converge poorly and are extremely sensitive to the interaction potential used in quantum scattering calculations. Despite these challenges, it was already shown that the fully quantum approach can accurately predict measured shifts not only for simpler systems involving hydrogen isotopologues [130–136], but also for O_2-perturbed HCl transitions [137] relevant to atmospheric applications. Furthermore, *ab initio* calculations provide a natural means of investigating the beyond-Voigt line-shape effects [132] and would not be subject to numerical correlations in the same way that advanced line-shape parameters derived from fitting spectra are. With these aforementioned prospects in mind, extensive theoretical investigations of various bands of O_2 (fine structure, rotational, electronic, e.g., A-band) were undertaken recently by the authors of Ref. [129], and new *ab initio* results concerning this molecule are to be expected in the near future.

3.5. Complications from competing high-pressure effects

Of the various visible and near-infrared O_2 absorption bands, the most prominent and probably the most important to remote sensing are the A- and 1.27 μm bands. Here we discuss current challenges to realizing self-consistent models of these monomeric bands that account for potentially confounding effects caused by contributions of collisional induced absorption (CIA), line mixing (LM) and intensity depletion (ID) –the latter effect caused by the breakdown of the impact approximation (BIA) (i.e. finite duration of collisions). All three of these mechanisms involve binary collisions, and therefore their magnitudes scale with the square of the total gas density. This quadratic dependence on density makes it difficult to completely disentangle these components in spectral analyses. Thus, strong constraints regarding their relative magnitudes and spectral shapes are required, but at present, all these data are usually not available. This problem is especially challenging in the case of the A-band, where the ratio of the collision-induced absorption (CIA) to monomer absorption is much smaller than for the 1.27 μm band.

Intensity depletion has been observed in absorption spectra of self- and foreign-broadened HCl [84,85,138], self-broadened CO_2 [139] and N_2-broadened CO [83]. It is manifest as a line-shape effect in which a small fraction of the intensity in the core of each line is redistributed to the far wings, while the overall intensity is conserved [83–85]. Indexing each line by i, this so-called core depletion is quantified by measuring the line area a_i (using standard line profiles based on the impact approximation such as the Hartmann-Tran profile or its reduced forms) and the O_2 number density, $n_{O2}(p,T)$, where p is total pressure and T is temperature. The ratio of these observables $a_i/n_{O2} = S_i(p,T)$, is interpreted as the apparent (core) intensity, which decreases linearly with the total number density, $n(p,T)$, of the gas mixture. Because the depletion coefficient, d_i, (typically expressed in units of amagat^{-1}) depends on T and gas composition, it is calculated from measurements (with these two conditions held constant) of a_i vs. $n(p,T)$, as $d_i = (1/S_i^{(0)}) dS_i/dn$, where $S_i^{(0)}$ is the actual (undepleted) line intensity obtained in the limit of zero pressure. Alternatively, this linear dependence of the core intensity on n, can be used as a constraint in a multi-spectrum fit of spectra acquired over a range of pressure. Note that in this context, an accurate real-gas equation of state should be used in the determinations of n and n_{O2} from measurements of pressure, temperature and composition [83]. Treating air as a binary mixture of O_2 and N_2 and assuming a small amount of depletion caused by binary collisions [140], we write the effective depletion coefficient in terms of the amount-fraction-weighted sum of the O_2–O_2 and O_2–N_2 depletion coefficients, $d_{i,O2-O2}$ and $d_{i,O2-N2}$ as

$$d_i = \chi_{O2} d_{i,O2-O2} + (1 - \chi_{O2}) d_{i,O2-N2}, \tag{9}$$

where χ_{O2} is the amount fraction of O_2 in air, nominally equal to 0.21.

With this working definition of intensity depletion, the contribution to the absorption coefficient associated with the line cores is obtained

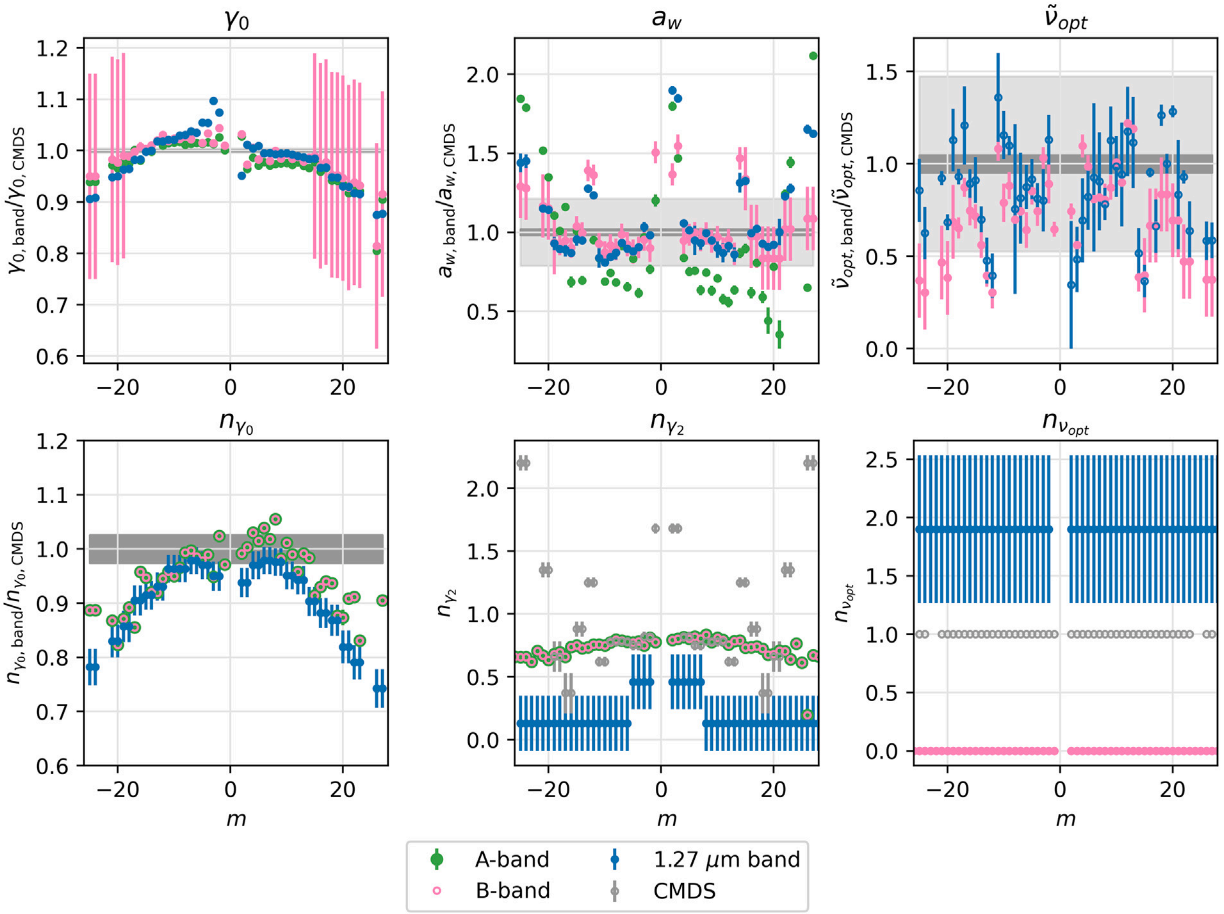

Fig. 13. Comparison between air-perturbed collisional broadening ($\gamma_{0,\mathrm{air}}$), speed-dependent broadening ($a_{w,\mathrm{air}}$), and Dicke narrowing parameters ($\tilde{\nu}_{opt,\mathrm{air}}$) and temperature dependencies as reported in HITRAN2024 [17] for the O_2 B- [99], A- [6], and 1.27 μm [48,61] bands and as determined by rCMDS [128]. Note, the n_{γ_0} and the n_{γ_2} values for the A- and B-bands are equal in HITRAN2024, leading to superposition of the component symbols.

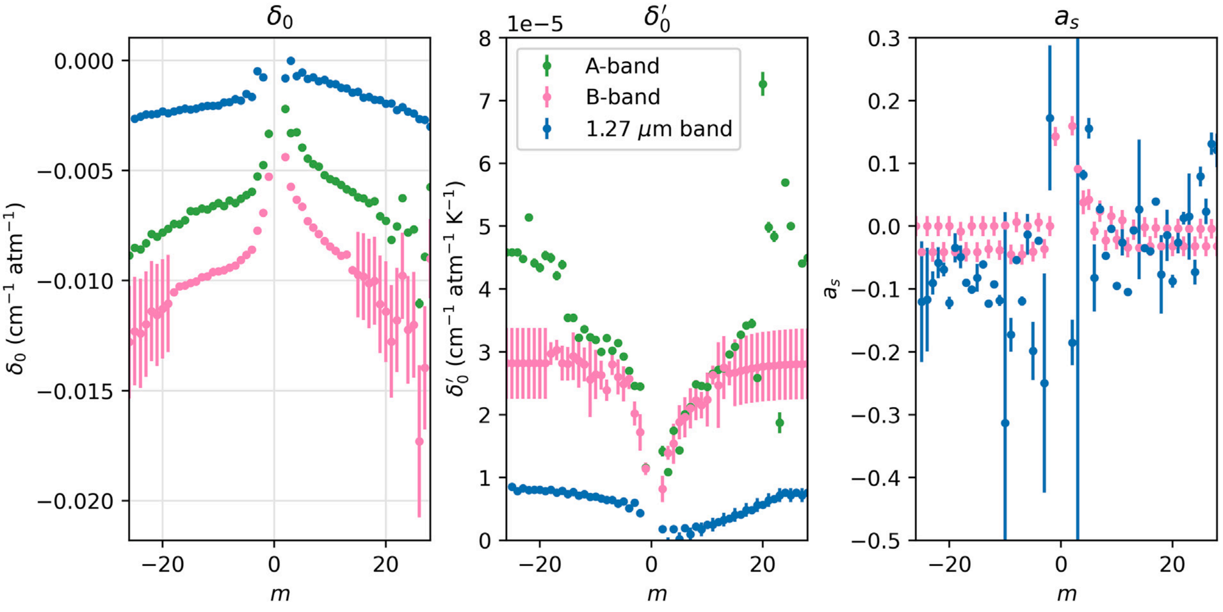

Fig. 14. Comparison between air-perturbed pressure shifting ($\delta_{0,\mathrm{air}}$), linear temperature dependence of pressure shifting ($\delta'_{0,\mathrm{air}}$), and speed-dependent shifting ($a_{s,\mathrm{air}}$) reported in HITRAN2024 [17] for the O_2 B- [99], A- [6], and 1.27 μm [48,61] bands.

by summing over all lines in the considered band. Adding the effect of first-order line mixing gives an absorption coefficient of

$$\alpha_{\mathrm{core}}(\tilde{\nu}) = \chi_{\mathrm{O2}} n \Sigma_i S_i^{(0)}[1 - nd_i][\boldsymbol{\Phi}^R_{i,\mathrm{core}}(\tilde{\nu} - \tilde{\nu}_{0,i}) + ny_i \boldsymbol{\Phi}^I_{i,\mathrm{core}}(\tilde{\nu} - \tilde{\nu}_{0,i})], \quad (10)$$

where $\tilde{\nu}_{0,i}$ is the line position, y_i is the first-order line mixing coefficient, and $\boldsymbol{\Phi}^{(R)}_{i,\mathrm{core}}$ and $\boldsymbol{\Phi}^{(I)}_{i,\mathrm{core}}$ are the real and imaginary components of the complex-valued profiles, $\tilde{\boldsymbol{\Phi}}_{i,\mathrm{core}}$, for the line cores, which depend implicitly on p, T, and gas composition through the variation of line-shape parameters with these quantities.

The resulting BIA spectrum caused by redistribution of intensity from all the line cores has a total intensity, S_{BIA}, equal to the sum of all the depleted core intensities, i.e., $S_{BIA}(p,T) = n\Sigma_i S_i^{(0)}(T)d_i(T)$. Because the BIA originates from binary collisions occurring on time scales much shorter than the average time between collisions [138], the resulting spectrum is relatively broad and comparable in width to the CIA spectrum, described below. One can write an expression analogous to Eq. (10) in terms of the depleted intensities, which includes absorption occurring on short collisional time scales and line mixing between these contributions. In this case, we approximate the line-shapes by a complex Lorentzian function, $\tilde{\boldsymbol{\Phi}}_{i,L} = \frac{1/\pi}{\Gamma_i - i(\tilde{\nu}-\tilde{\nu}_o)}$ with a halfwidth Γ_i given by $1/2\pi c\tau_i$ where τ_i is the line-dependent collision duration [138]. Summing over all transitions and assuming the same line mixing coefficients as above, the absorption coefficient for the BIA spectrum is,

$$\begin{aligned}\alpha_{\mathrm{BIA}}(\tilde{\nu}) &= \chi_{\mathrm{O2}} n \Sigma_i S_i^{(0)} nd_i[\boldsymbol{\Phi}^R_{i,L}(\tilde{\nu} - \tilde{\nu}_{0,i}) + ny_i \boldsymbol{\Phi}^I_{i,L}(\tilde{\nu} - \tilde{\nu}_{0,i})] \\ &= \chi_{\mathrm{O2}} n S_{\mathrm{BIA}}[\boldsymbol{\Phi}_{\mathrm{BIA}}(\tilde{\nu}) + \boldsymbol{\Phi}'_{\mathrm{BIA}}(\tilde{\nu})],\end{aligned} \quad (11)$$

in which $\boldsymbol{\Phi}^R_{i,L}$ and $\boldsymbol{\Phi}^I_{i,L}$ are the real and imaginary components of $\tilde{\boldsymbol{\Phi}}_{i,L}$. In Eq. (11), $\boldsymbol{\Phi}_{\mathrm{BIA}} = \sum S_i^{(0)} nd_i \boldsymbol{\Phi}^R_i / S_{\mathrm{BIA}}$ and $\boldsymbol{\Phi}'_{\mathrm{BIA}} = \sum S_i^{(0)} n^2 y_i d_i \boldsymbol{\Phi}^I_i / S_{\mathrm{BIA}}$, which satisfy $\int \boldsymbol{\Phi}_{\mathrm{BIA}} d\tilde{\nu} = 1$ and $\int \boldsymbol{\Phi}'_{\mathrm{BIA}} d\tilde{\nu} = 0$. Although the line mixing term proportional to $\boldsymbol{\Phi}'_{\mathrm{BIA}}$ has a net spectrum area of zero, it could be difficult to distinguish from the broadband BIA ($\boldsymbol{\Phi}_{\mathrm{BIA}}$ term) and CIA spectra. Nevertheless, the magnitude of the line mixing term in Eq. (11) is third order in density, indicating that for low pressure one can safely assume that $|\boldsymbol{\Phi}'_{\mathrm{BIA}}|/\boldsymbol{\Phi}_{\mathrm{BIA}} \ll 1$ so that this contribution to the BIA would be negligible.

For the O_2-air CIA, we make the same binary mixture approximation as above for the BIA. Summing contributions from O_2–O_2 and O_2–N_2 collisions gives,

$$\alpha_{\mathrm{CIA}}(\tilde{\nu}) = n^2[\chi^2_{\mathrm{O2}} B_{\mathrm{O2-O2}}(\tilde{\nu}) + \chi_{\mathrm{O2}}(1 - \chi_{\mathrm{O2}}) B_{\mathrm{O2-N2}}(\tilde{\nu})] \quad (12)$$

where $B_{\mathrm{O2-O2}}$ and $B_{\mathrm{O2-N2}}$ are the broadband binary absorption coefficient spectra for the respective collisional pairs.

Measurements of CIA in the A- and 1.27 μm bands of O_2-O_2, O_2–N_2- and O_2-air are discussed in [82,141–145] along with *ab initio* calculations of band shapes [146] providing the basis for parameterized models anchored to measured spectra [147].

The net absorption coefficient, $\alpha(\tilde{\nu})$ is obtained by adding Eqs. (10), (11), (12) to give

$$\alpha(\tilde{\nu}) = \alpha_{\mathrm{core}}(\tilde{\nu}) + \alpha_{\mathrm{BIA}}(\tilde{\nu}) + \alpha_{\mathrm{CIA}}(\tilde{\nu}), \quad (13)$$

all of which have terms that are quadratic in density because of the LM, BIA, and CIA contributions. Only the component in α_{core} given by $\chi_{\mathrm{O2}} n \Sigma_i S_i^{(0)} \boldsymbol{\Phi}^{(R)}_{i,core}$ (which represents the monomer spectrum in the limit of zero pressure) is linearly proportional to density at a given temperature.

At present, there is much disagreement among theoretical and experimental spectral shapes of CIA in the A-band region [82,146]. Experimentally, spectra are analyzed by modeling absorption from monomer lines and line mixing, with the CIA spectrum being assigned to fit residuals. With this empirical approach, the resulting CIA spectra are quite sensitive to the choice of line mixing model (e.g., first-order Rosenkranz coefficients, partial- or full-matrix line mixing, etc.). Perhaps most importantly, no prior studies included theoretical constraints on the shape of the CIA spectrum nor the above-mentioned effects of intensity depletion (BIA spectrum). We conclude that improved agreement between measurements, as well as between experiment and theory, requires a more comprehensive analytical approach than has been so far demonstrated.

The preceding formalism should be a useful framework supporting the development and realization of a predictive, self-consistent absorption model for air-broadened O_2 spectra appropriate for application over a wide pressure and temperature range. In general, the separation of the LM, CIA, and BIA components that vary quadratically with pressure continues to be especially challenging. We expect that differences in the temperature dependencies of the band intensities for the CIA and BIA, as well as their spectral shapes ($\boldsymbol{\Phi}_{\mathrm{CIA}}$ and $\boldsymbol{\Phi}_{\mathrm{BIA}}$) and composition dependencies, can be exploited to precisely separate these effects. Furthermore, in principle, the imaginary component of the line mixing coefficient (which is typically ignored in nearly all analyses) can increase or decrease the integrated area of the real part of the line profile, making it difficult to distinguish from the intensity depletion effect described here [148]. Achieving this level of understanding requires more experiments and theoretical calculations (e.g., see classical molecular dynamics simulations of [138]) to experimentally confirm theoretical predictions, and thereby establish robust constraints for this model. Both high-resolution line-by-line studies and broadband determinations of the underlying BIA and CIA contributions are needed, and better experimental characterization and theoretical understanding of the J dependence and band-to-band differences in the intensity depletion coefficients are required. For the line mixing terms, using a full-matrix model with proper temperature normalization [142] might be necessary and would ensure that the line mixing is properly constrained. Because CIA within the 1.27 μm band is relatively prominent by comparison to the monomer lines, the broad BIA spectrum should be relatively weak compared to that of the CIA. Thus, complications due to the overlapping BIA and CIA components are expected to be less severe than in the A-band.

4. Conclusions

We have provided an overview of measurements and supporting theoretical calculations of the updated O_2 line parameters included in the 2024 edition of the HITRAN database [17]. These results include the intensities of electric quadrupole rotational lines within the ground electronic state, Einstein A parameters needed to model radiant emission in the excited-state Noxon band, and intensities of A-band transitions relevant to remote sensing of atmospheric surface pressure. These updates also included revised line positions and advanced line-shape parameters in the 1.27 μm and B-bands of O_2 as well as updates to the Schumann-Runge bands linewidths to address inconsistencies (with respect to literature data) in prior editions of HITRAN.

Looking ahead, we have also discussed scientific gaps and recommended research strategies involving O_2 spectroscopic data that go beyond the new parameters given in HITRAN2024 [17]. This outlook section includes a discussion of the definition of standard air mixtures for spectroscopic measurements, the need for *ab initio* line intensities in modeling measured spectra, the comparison of air-broadened line-shape parameters across various bands, and the importance of experimental validation of theoretical line-shape parameters. Finally, we discussed challenges in the measurement and modeling of concurrent binary collision effects in O_2 spectra, which are important at elevated gas pressure.

CRediT authorship contribution statement

Erin M. Adkins: Writing – review & editing, Writing – original draft, Visualization, Investigation, Formal analysis, Conceptualization. **Joseph T. Hodges:** Writing – review & editing, Writing – original draft, Visualization. **Katarzyna Bielska:** Writing – review & editing, Writing – original draft, Investigation, Formal analysis. **Alain Campargue:**

Writing – review & editing, Investigation. **Roman Ciuryło:** Investigation. **Jolanta Domysławska:** Investigation. **Rafael P. Fernandez:** Investigation. **Hélène Fleurbaey:** Investigation. **Maciej Gancewski:** Writing – original draft, Visualization, Investigation. **Hubert Jóźwiak:** Investigation. **Samir Kassi:** Investigation. **Daniel Lisak:** Writing – review & editing, Investigation. **Didier Mondelain:** Writing – original draft, Investigation, Formal analysis. **Gustavo G. Palancar:** Investigation. **Wilfrid Somogyi:** Investigation. **Orlando G. Tomazzeli:** Writing – original draft, Visualization, Investigation. **Ha Tran:** Writing – review & editing, Writing – original draft, Investigation. **Piotr Wcisło:** Writing – review & editing, Writing – original draft, Investigation. **Szymon Wójtewicz:** Investigation. **Sergei N. Yurchenko:** Investigation. **Iouli E. Gordon:** Writing – review & editing, Writing – original draft, Supervision, Investigation, Conceptualization.

Declaration of competing interest

The authors declare that they have no known competing financial interests or personal relationships that could have appeared to influence the work reported in this paper.

Acknowledgments

EMA and JTH acknowledge funding from the NIST Greenhouse Gas and Climate Science Program and the National Aeronautics and Space Administration (NASA) [contract NNH20ZDA0001N-OCOT].

We acknowledge support by the National Science Centre in Poland through project no. 2023/51/B/ST2/00427 (D.L.), 2018/30/E/ST2/00864 (K.B.), 2018/29/B/ST2/02974 (J.D.), 2019/35/B/ST2/01118 (H.J.), 2022/46/E/ST2/00282 (P.W.). M.G. was supported by the Polish Ministry of Science and Higher Education through Project No. PN/01/0229/2022 under the “Perły Nauki” program. For the purpose of Open Access, the authors has applied a CC-BY public copyright licence to any Author Accepted Manuscript (AAM) version arising from this submission. We gratefully acknowledge Polish high-performance computing infrastructure PLGrid (HPC Center: ACK Cyfronet AGH) for providing computer facilities and support within computational grant no. PLG/2024/017376. Created using resources provided by Wroclaw Centre for Networking and Supercomputing (http://wcss.pl).

The contribution of the Grenoble group (A.C., H.F., D.M., S.K.) was supported by CNES, France in the frame of the MicroCarb project (CNES specific agreement #231398/00).

The HITRAN database is supported by NASA, United States grant 80NSSC23K1596.

The authors would like to thank Eisen Gross (NIST) and Jasper Stroud (NIST) for commenting on the manuscript.

Appendix A. Supplementary data

Supplementary material related to this article can be found online at https://doi.org/10.1016/j.jqsrt.2025.109629.

Data availability

Data will be made available on request.

References

[1] Atkinson R. Reactions of oxygen species in the atmosphere. In: Active oxygen in chemistry. vol. 2, Springer Netherlands; 1995, p. 249–79. http://dx.doi.org/10.1007/978-94-007-0874-7_7", Ch. 7.

[2] Mlynczak MG, Marshall BT. A reexamination of the role of solar heating in the O_2 atmospheric and infrared atmospheric bands. Geophys Res Lett 1996;23(6):657–60. http://dx.doi.org/10.1029/96GL00145.

[3] Babcock GT. How oxygen is activated and reduced in respiration. Proc Natl Acad Sci 1999;96(23):12971–3. http://dx.doi.org/10.1073/pnas.96.23.12971.

[4] O'Brien DM, Mitchell RM, English SA, Costa GAD. Airborne measurements of air mass from O_2 A-band absorption spectra. J Atmos Ocean Technol 1998;15(6):1272–86. http://dx.doi.org/10.1175/1520-0426(1998)015<1272:AMOAMF>2.0.CO;2.

[5] van Diedenhoven B, Hasekamp OP, Aben I. Surface pressure retrieval from SCIAMACHY measurements in the O_2 A band: Validation of the measurements and sensitivity on aerosols. Atmos Chem Phys 2005;5(8):2109–20. http://dx.doi.org/10.5194/acp-5-2109-2005.

[6] Payne VH, Drouin BJ, Oyafuso F, Kuai L, Fisher BM, Sung K, Nemchick D, Crawford TJ, Smyth M, Crisp D, et al. Absorption coefficient (ABSCO) tables for the Orbiting Carbon Observatories: Version 5.1. J Quant Spectrosc Radiat Transfer 2020;255:107217. http://dx.doi.org/10.1016/j.jqsrt.2020.107217.

[7] Kuze A, Chance KV. Analysis of cloud top height and cloud coverage from satellites using the O_2 A- and B-bands. J Geophys Res: Atmos 1994;99(D7):14481–91. http://dx.doi.org/10.1029/94JD01152.

[8] Li Q, Sun X, Wang X. Cloud phase recognition based on oxygen A-band and CO_2 1.6 μm-band. Remote Sens 2021;13(9). http://dx.doi.org/10.3390/rs13091681.

[9] Zinner T, Schwarz U, Kölling T, Ewald F, Jäkel E, Mayer B, Wendisch M. Cloud geometry from oxygen A-band observations through an aircraft side window. Atmos Meas Tech 2019;12(2):1167–81. http://dx.doi.org/10.5194/amt-12-1167-2019.

[10] Colosimo SF, Natraj V, Sander SP, Stutz J. A sensitivity study on the retrieval of aerosol vertical profiles using the oxygen A-band. Atmos Meas Tech 2016;9(4):1889–905. http://dx.doi.org/10.5194/amt-9-1889-2016.

[11] Nowlan CR, McElroy CT, Drummond JR. Measurements of the O_2 A- and B-bands for determining temperature and pressure profiles from ACE–MAESTRO: Forward model and retrieval algorithm. J Quant Spectrosc Radiat Transfer 2007;108(3):371–88. http://dx.doi.org/10.1016/j.jqsrt.2007.06.006.

[12] Stevens MH, Englert CR, Harlander J, et al. Temperatures in the upper mesosphere and lower thermosphere from O_2 atmospheric band emission observed by ICON/MIGHTI. Space Sci Rev 2022;218:67. http://dx.doi.org/10.1007/s11214-022-00935-x.

[13] Sun K, Yousefiand M, Millerand CC, Chance K, Abad GG, Gordon IE, Liu X, O'Sullivan E, Sioris CE, Wofsy SC. An optimal estimation-based retrieval of upper atmospheric oxygen airglow and temperature from SCIAMACHY limb observations. Atmos Meas Tech 2022;15:3721–45. http://dx.doi.org/10.5194/amt-15-3721-2022.

[14] Airapetian VS, Jackman CH, M. Mlynczak M, et al. Atmospheric beacons of life from exoplanets around G and K stars. Sci Rep 2017;7:14141. http://dx.doi.org/10.1038/s41598-017-14192-4.

[15] Rukdee S. Instrumentation prospects for rocky exoplanet atmospheres studies with high resolution spectroscopy. Sci Rep 2024;14:27356. http://dx.doi.org/10.1038/s41598-024-78071-5.

[16] Drouin BJ, Yu S, Miller CE, Müller HSP, Lewen F, Brünken S, Habara H. Terahertz spectroscopy of oxygen, O_2, in its $^3\Sigma_g^-$ and $^1\Delta$ electronic states: THz spectroscopy of O_2. J Quant Spectrosc Radiat Transfer 2010;111(9):1167–73. http://dx.doi.org/10.1016/j.jqsrt.2009.12.006.

[17] Gordon IE. The HITRAN2024 molecular spectroscopic database. JQSRT 2025. in prepartion.

[18] Yu S, Miller CE, Drouin BJ, Müller HSP. High resolution spectral analysis of oxygen. IV. Energy levels, partition sums, band constants, RKR potentials, Franck-Condon factors involving the $X^3\Sigma_g^-$, $a^1\Delta_g$ and $b^1\Sigma_g^+$ states. J Chem Phys 2014;141:174302. http://dx.doi.org/10.1063/1.4900510.

[19] Cosby PC, Park H, Copeland RA, Slanger TG. Predissociation linewidths in O_2 B $^3\Sigma_u^-$ -(v= 0, 2). J Chem Phys 1993;98(7):5117–33. http://dx.doi.org/10.1063/1.464941.

[20] Vroonhoven MCGNv. Theory and calculations on the Herzberg states of the oxygen molecule. Sl: sn; 2003.

[21] Hill C, Gordon IE, Kochanov RV, Barrett L, Wilzewski JS, Rothman LS. HITRANonline: An online interface and the flexible representation of spectroscopic data in the HITRAN database. J Quant Spectrosc Radiat Transfer 2016;177:4–14. http://dx.doi.org/10.1016/j.jqsrt.2015.12.012.

[22] Tennyson J, Bernath PF, Campargue A, Császár AG, Daumont L, Gamache RR, Hodges JT, Lisak D, Naumenko OV, Rothman LS, Tran H, Zobov NF, Buldyreva J, Boone CD, Vizia MDD, Gianfrani L, Hartmann J-M, McPheat R, Weidmann D, Murray J, Ngo NH, Polyansky OL. Recommended isolated-line profile for representing high-resolution spectroscopic transitions (IUPAC technical report). Pure Appl Chem 2014;86(12):1931–43. http://dx.doi.org/10.1515/pac-2014-0208.

[23] Ngo NH, Lisak D, Tran H, Hartmann J-M. An isolated line-shape model to go beyond the Voigt profile in spectroscopic databases and radiative transfer codes. J Quant Spectrosc Radiat Transfer 2013;129:89–100. http://dx.doi.org/10.1016/j.jqsrt.2013.05.034.

[24] Kochanov RV, Gordon IE, Rothman LS, Wcisło P, Hill C, Wilzewski JS. HITRAN application programming interface (HAPI): A comprehensive approach to working with spectroscopic data. J Quant Spectrosc Radiat Transfer 2016;177:15–30. http://dx.doi.org/10.1016/j.jqsrt.2016.03.005.

[25] Wcislo P, Stolarczyk N, Slowinski M, Jozwiak H, Lisak D, Ciurylo R, Cygan A, Schreier F, Boone CD, Castrillo A, Gianfrani L, Tan Y, Hu S-M, Adkins EM, Hodges JT, Tran H, Ngo HN, Hartmann J-M, Beguier S, Campargue A, Hargreaves RJ, Rothman LS, Gordon IE. New beyond-voigt line-shape profile recommended for the HITRAN database. Journal of Quantitative Spectroscopy and Radiative Transfer 2025;109596. http://dx.doi.org/10.1016/j.jqsrt.2025.109596.

[26] Rosenkranz P. Shape of the 5 mm oxygen band in the atmosphere. IEEE Trans Antennas and Propagation 1975;23(4):498–506. http://dx.doi.org/10.1109/TAP.1975.1141119.

[27] Gancewski M, Jóźwiak H, Cybulski H, Wcisło P. Intensities of all fine-structure resolved rovibrational electric quadrupole absorption lines in $^{16}O_2(X^3\Sigma_g^-)$ calculated with a new *ab initio* quadrupole moment curve. J Quant Spectrosc Radiat Transfer 2025;337:109395. http://dx.doi.org/10.1016/j.jqsrt.2025.109395.

[28] Werner H-J, Knowles PJ, Knizia G, Manby FR, Schütz M, et al. MOLPRO, version 2022.2, a package of ab initio programs. 2022, http://www.molpro.net.

[29] Dunning Jr TH. Gaussian basis sets for use in correlated molecular calculations. I. The atoms boron through neon and hydrogen. J Chem Phys 1989;90:1007–23. http://dx.doi.org/10.1063/1.456153.

[30] Lill JV, Parker GA, Light JC. Discrete variable representations and sudden models in quantum scattering theory. Chem Phys Lett 1982;89:483–9. http://dx.doi.org/10.1016/0009-2614(82)83051-0.

[31] Light JC, Hamilton IP, Lill JV. Generalized discrete variable approximation in quantum mechanics. J Chem Phys 1985;82:1400–9. http://dx.doi.org/10.1063/1.448462.

[32] Bytautas L, Matsunaga N, Ruedenberg K. Accurate *ab initio* potential energy curve of O_2. II. Core-valence correlations, relativistic contributions, and vibration-rotation spectrum. J Chem Phys 2010;132:074307. http://dx.doi.org/10.1063/1.3298376.

[33] Medvedev ES, Meshkov VV, Stolyarov AV, Gordon IE. Peculiarities of high-overtone transition probabilities in carbon monoxide revealed by high-precision calculation. J Chem Phys 2015;143:154301. http://dx.doi.org/10.1063/1.4933136.

[34] Medvedev ES, Meshkov VV, Stolyarov AV, Ushakov VG, Gordon IE. Impact of the dipole-moment representation on the intensity of high overtones. J Mol Spectrosc 2016;330:36–42. http://dx.doi.org/10.1016/j.jms.2016.06.013.

[35] Meshkov VV, Stolyarov AV, Ermilov AYu, Medvedev ES, Ushakov VG, Gordon IE. Semi-empirical ground-state potential of carbon monoxide with physical behavior in the limits of small and large inter-atomic separations. J Quant Spectrosc Radiat Transfer 2018;217:262–73. http://dx.doi.org/10.1016/j.jqsrt.2018.06.001.

[36] Meshkov VV, Ermilov AYu, Stolyarov AV, Medvedev ES, Ushakov VG, Gordon IE. Semi-empirical dipole moment of carbon monoxide and line lists for all its isotopologues revisited. J Quant Spectrosc Radiat Transfer 2022;280:108090. http://dx.doi.org/10.1016/j.jqsrt.2022.108090.

[37] Medvedev ES, Ushakov VG. Irregular semi-empirical dipole-moment function for carbon monoxide and line lists for all its isotopologues verified for extremely high overtone transitions. J Quant Spectrosc Radiat Transfer 2022;288:108255. http://dx.doi.org/10.1016/j.jqsrt.2022.108255.

[38] Ushakov VG, Semenov M, Yurchenko SN, Ermilov AYu, Medvedev ES. Improved potential-energy and dipole-moment functions of the ground electronic state of phosphorus nitride. J Mol Spectrosc 2023;395:111804. http://dx.doi.org/10.1016/j.jms.2023.111804.

[39] Medvedev ES. Determination of a new molecular constant from overtone vibrational spectra. J Mol Spectrosc 1985;114:1–12. http://dx.doi.org/10.1016/0022-2852(85)90330-3.

[40] Gordon IE, Rothman LS, Hargreaves RJ, Hashemi R, Karlovets EV, Skinner FM, Conway EK, Hill C, Kochanov RV, Tan Y, Wcisło P, Finenko AA, Nelson K, Bernath PF, Birk M, Boudon V, Campargue A, Chance KV, Coustenis A, Drouin BJ, Flaud JM, Gamache RR, Hodges JT, Jacquemart D, Mlawer EJ, Nikitin AV, Perevalov V, Rotger M, Tennyson J, Toon GC, Tran H, Tyuterev VG, Adkins EM, Baker A, Barbe A, Canè E, Császár AG, Dudaryonok A, Egorov O, Fleisher AJ, Fleurbaey H, Foltynowicz A, Furtenbacher T, Harrison JJ, Hartmann JM, Horneman VM, Huang X, Karman T, Karns J, Kassi S, Kleiner I, Kofman V, Kwabia-Tchana F, Lavrentieva NN, Lee TJ, Long DA, Lukashevskaya AA, Lyulin OM, Makhnev VY, Matt W, Massie ST, Melosso M, Mikhailenko SN, Mondelain D, Müller HSP, Naumenko OV, Perrin A, Polyansky OL, Raddaoui E, Raston PL, Reed ZD, Rey M, Richard C, Tóbiás R, Sadiek I, Schwenke DW, Starikova E, Sung K, Tamassia F, Tashkun SA, Vander Auwera J, Vasilenko IA, Vigasin AA, Villanueva GL, Vispoel B, Wagner G, Yachmenev A, Yurchenko SN. The HITRAN2020 molecular spectroscopic database. J Quant Spectrosc Radiat Transfer 2022;277:107949. http://dx.doi.org/10.1016/j.jqsrt.2021.107949.

[41] Balasubramanian TK, Bellary VP, Rao KN. Branch intensities in the magnetic dipole rotation–vibration spectrum of the oxygen molecule. Can J Phys 1994;72:971–8. http://dx.doi.org/10.1139/p94-128.

[42] Noxon JF. Observation of the $b^1\Sigma_g - a^1\Delta_g$ transition in O_2. Can J Phys 1961;39:1110–9. http://dx.doi.org/10.1139/p61-126.

[43] Gordon I, Mondelain D, Kassi S, Campargue A, Fleurbaey H, Long D, Hodges J. Disentangling magnetic dipole and electric quadrupole intensity contributions in spectra of molecular oxygen at 1.27 μ m. updated line positions and intensities. JQSRT 2025. in preparation.

[44] Ionin AA, Kochetov IV, Napartovich AP, Yuryshev NN. Physics and engineering of singlet delta oxygen production in low-temperature plasma. J Phys D: Appl Phys 2007;40:R25–61. http://dx.doi.org/10.1088/0022-3727/40/2/R01.

[45] Sun K, Gordon IE, Sioris CE, Liu X, Chance K, Wofsy SC. Reevaluating the use of O_2 $a^1\Delta_g$ band in spaceborne remote sensing of greenhouse gases. Geophys Res Lett 2018;45:5779–87. http://dx.doi.org/10.1029/2018GL077823.

[46] Tran DD, Tran H, Vasilchenko S, Kassi S, Campargue A, Mondelain D. High sensitivity spectroscopy of the O_2 band at 1.27 μm: (II) air-broadened line profile parameters. J Quant Spectrosc Radiat Transfer 2020;240:106673. http://dx.doi.org/10.1016/j.jqsrt.2019.106673.

[47] Konefał M, Kassi S, Mondelain D, Campargue A. High sensitivity spectroscopy of the O2 band at 1.27 μm:(I) pure O_2 line parameters above 7920 cm^{-1}. J Quant Spectrosc Radiat Transfer 2020;241:106653. http://dx.doi.org/10.1016/j.jqsrt.2019.106653.

[48] Fleurbaey H, Reed ZD, Adkins EM, Long DA, Hodges JT. High accuracy spectroscopic parameters of the 1.27 μm band of O_2 measured with comb-referenced, cavity ring-down spectroscopy. J Quant Spectrosc Radiat Transfer 2021;270:107684. http://dx.doi.org/10.1016/j.jqsrt.2021.107684.

[49] Leshchishina O, Kassi S, Gordon IE, Yu S, Campargue A. The $a^1\Delta_g - X^3\Sigma_g^-$ band of $^{16}O^{17}O$, $^{17}O^{18}O$ and $^{17}O_2$ by high sensitivity CRDS near 1.27μm. J Quant Spectrosc Radiat Transfer 2011;112(8):1257–65. http://dx.doi.org/10.1016/j.jqsrt.2011.01.014.

[50] Koshelev MA, Golubiatnikov GY, Vilkov IN, Tretyakov MY. Molecular oxygen fine structure with sub-kHz accuracy. J Quant Spectrosc Radiat Transfer 2022;278:108001. http://dx.doi.org/10.1016/j.jqsrt.2021.108001.

[51] Drouin BJ, Gupta H, Yu S, Miller CE, Müller HSP. High resolution spectral analysis of oxygen. II. Rotational spectra of $a^1\Delta_g$ O_2 isotopologues. J Chem Phys 2012;137(2):024305. http://dx.doi.org/10.1063/1.4719169.

[52] Drouin BJ, Yu S, Elliott BM, Crawford TJ, Miller CE. High resolution spectral analysis of oxygen. III. Laboratory investigation of the airglow bands. J Chem Phys 2013;139(14):144301. http://dx.doi.org/10.1063/1.4821759.

[53] Endo Y, Mizushima M. Microwave resonance lines of $^{16}O_2$ in its electronic ground state ($X^3\Sigma_g^-$). Japan J Appl Phys 1982;21(6A):L379. http://dx.doi.org/10.1143/JJAP.21.L379.

[54] Golubiatnikov GY, Krupnov AF. Microwave study of the rotational spectrum of oxygen molecule in the range up to 1.12 THz. J Mol Spectrosc 2003;217(2):282–7. http://dx.doi.org/10.1016/s0022-2852(02)00058-9.

[55] Zink LR, Mizushima M. Pure rotational far-infrared transitions of $^{16}O_2$ in its electronic and vibrational ground state. J Mol Spectrosc 1987;125(1):154–8. http://dx.doi.org/10.1016/0022-2852(87)90201-3.

[56] Nieh JC, Valentini JJ. Molecular potentials from CARS photofragment spectroscopy: spectroscopic constants and potential energy curve for oxygen ($a^1\Delta_g$). J Phys Chem 1987;91(6):1370–4. http://dx.doi.org/10.1021/j100290a020.

[57] Rouillé G, Millot G, Saint-Loup R, Berger H. High-resolution stimulated Raman spectroscopy of O_2. J Mol Spectrosc 1992;154(2):372–82. http://dx.doi.org/10.1016/0022-2852(92)90215-A.

[58] Mondelain D, Kassi S, Sala T, Romanini D, Gatti D, Campargue A. Sub-MHz accuracy measurement of the S(2) 2–0 transition frequency of D2 by comb-assisted cavity ring down spectroscopy. J Mol Spectrosc 2016;326:5–8. http://dx.doi.org/10.1016/j.jms.2016.02.008.

[59] Mondelain D, Mikhailenko SN, Karlovets EV, Béguier S, Kassi S, Campargue A. Comb-assisted cavity ring down spectroscopy of ^{17}O enriched water between 7443 and 7921 cm^{-1}. J Quant Spectrosc Radiat Transfer 2017;203:206–12. http://dx.doi.org/10.1016/j.jqsrt.2017.03.029.

[60] Long DA, Wójtewicz S, Miller CE, Hodges JT. Frequency-agile, rapid scanning cavity ring-down spectroscopy (FARS-CRDS) measurements of the (30012)-(00001) near-infrared carbon dioxide band. J Quant Spectrosc Radiat Transfer 2015;161:35–40. http://dx.doi.org/10.1016/j.jqsrt.2015.03.031.

[61] Klemm J, Campargue A, Fleurbaey H, Kassi S, Romanini D, Mondelain D. Temperature dependence of the air-broadened line-shape parameters of the 1.27 μm O_2-band. J Quant Spectrosc Radiat Transfer 2025;342:109448. http://dx.doi.org/10.1016/j.jqsrt.2025.109448.

[62] Newville M, Otten R, Nelson A, Stensitzki T, Ingargiola A, Allan D, Fox A, Carter F, Rawlik M. LMFIT: Non-linear least-squares minimization and curve-fitting for python. 2025, http://dx.doi.org/10.5281/zenodo.15014437.

[63] Hartmann J-M. A simple empirical model for the collisional spectral shift of air-broadened CO_2 lines. J Quant Spectrosc Radiat Transfer 2009;110(18):2019–26. http://dx.doi.org/10.1016/j.jqsrt.2009.05.016.

[64] Adkins EM, Yurchenko SN, Somogyi W, Hodges JT. An accurate determination of O_2 A-band line intensities through experiment and theory. JQSRT 2025;338:109412. http://dx.doi.org/10.1016/j.jqsrt.2025.109412.

[65] Somogyi W, Yurchenko SN, Kim G-S. An *ab initio* spectroscopic model of the molecular oxygen atmospheric and infrared bands. Phys Chem Chem Phys 2024;26:27419–30. http://dx.doi.org/10.1039/D4CP02619E.

[66] Watson JKG. Rotational line intensities in $3\Sigma-1\Sigma$ electronic transitions. Can J Phys 1968;46(14):1637–43. http://dx.doi.org/10.1139/p68-491.

[67] Watson JKG. Quadratic Herman–Wallis factors in the fundamental bands of linear molecules. J Mol Spectrosc 1987;125(2):428–41. http://dx.doi.org/10.1016/0022-2852(87)90108-1.

[68] Long DA, Havey DK, Okumura M, Miller CE, Hodges JT. O_2 A-band line parameters to support atmospheric remote sensing. J Quant Spectrosc Radiat Transfer 2010;111(14):2021–36. http://dx.doi.org/10.1016/j.jqsrt.2010.05.011.

[69] Fleurbaey H, Yi H, Adkins EM, Fleisher AJ, Hodges JT. Cavity ring-down spectroscopy of CO_2 near λ=2.06 μm: Accurate transition intensities for the Orbiting Carbon Observatory-2 (OCO-2) "strong band". J Quant Spectrosc Radiat Transfer 2020;252:107104. http://dx.doi.org/10.1016/j.jqsrt.2020.107104.

[70] Rothman LS, Rinsland CP, Goldman A, Massie ST, Edwards DP, Flaud J-M, Perrin A, Camy-peyret C, Dana V, Mandin J-Y, Schroeder J, Mccann A, Gamache RR, Wattson RB, Yoshino K, Chance KV, Jucks KW, Brown LR, Nemtchinov V, Varanasi P. The HITRAN molecular spectroscopic database and hawks (HITRAN atmospheric workstation): 1996 edition. J Quant Spectrosc Radiat Transfer 2001;60:665–710. http://dx.doi.org/10.1016/S0022-4073(98)00078-8.

[71] Rothman LS, Barbe A, Benner DC, Brown LR, Camy-Peyret C, Carleer MR, Chance K, Clerbaux C, Dana V, Devi VM, et al. The HITRAN molecular spectroscopic database: edition of 2000 including updates through 2001. J Quant Spectrosc Radiat Transfer 2003;82(1):5–44. http://dx.doi.org/10.1016/S0022-4073(03)00146-8.

[72] Rothman LS, Jacquemart D, Barbe A, Benner DC, Birk M, Brown LR, Carleer MR, Chackerian Jr C, Chance K, Coudert LH, et al. The HITRAN 2004 molecular spectroscopic database. J Quant Spectrosc Radiat Transfer 2005;96(2):139–204. http://dx.doi.org/10.1016/j.jqsrt.2004.10.008.

[73] Rothman LS, Gordon IE, Barbe A, Benner DC, Bernath PF, Birk M, Boudon V, Brown LR, Campargue A, Champion J-P, Chance K, Coudert LH, Dana V, Devi VM, Fally S, Flaud J-M, Gamache RR, Goldman A, Jacquemart D, Kleiner I, Auwera JV. The HITRAN 2008 molecular spectroscopic database. J Quant Spectrosc Radiat Transfer 2009;110:533–72. http://dx.doi.org/10.1016/j.jqsrt.2009.02.013.

[74] Rothman LS, Gordon IE, Babikov Y, Barbe A, Benner DC, Bernath PF, Birk M, Bizzocchi L, Boudon V, Brown LR, Campargue A, Chance K, Cohen EA, Coudert LH, Devi VM, Drouin BJ, Fayt A, Flaud J-M, Gamache RR, Harrison JJ, f GW. The HITRAN2012 molecular spectroscopic database. J Quant Spectrosc Radiat Transfer 2013;130:4–50. http://dx.doi.org/10.1016/j.jqsrt.2013.07.002.

[75] Gordon IE, Rothman LS, Hill C, Kochanov RV, Tan Y, Bernath PF, Birk M, Boudon V, Campargue A, Chance KV, Drouin BJ, Flaud J-M, Gamache RR, Hodges JT, Jacquemart D, Perevalov VI, Perrin A, Shine KP, Smith M-A, Tennyson J, Toon GC, Tran H, Tyuterev VG, Barbe A, Császár AG, Devi VM, Furtenbacher T, Harrison JJ, Hartmann J-M, Jolly A, Johnson TJ, Karman T, Kleiner I, Kyuberis AA, Loos J, Lyulin OM, Massie ST, Mikhailenko SN, Moazzen-Ahmadi N, Müller HSP, Naumenko OV, Nikitin AV, Polyansky OL, Rey M, Rotger M, Sharpe SW, Sung K, Starikova E, Tashkun SA, Auwera JV, abd J. Wilzewski GW, Wcisło P, Yu S, Zak EJ. The HITRAN2016 molecular spectroscopic database. J Quant Spectrosc Radiat Transfer 2017;203:3–69. http://dx.doi.org/10.1016/j.jqsrt.2017.06.038.

[76] Ritter KJ, Wilkerson TD. High-resolution spectroscopy of the oxygen A band. J Mol Spectrosc 1987;121(1):1–19. http://dx.doi.org/10.1016/0022-2852(87)90167-6.

[77] Miller JH, Boese RW, Giver LP. Intensity measurements and rotational intensity distribution for the oxygen A-band. J Quant Spectrosc Radiat Transfer 1969;9(11):1507–17. http://dx.doi.org/10.1016/0022-4073(69)90021-1.

[78] Galkin VD. Electronic moment of the $b' \Sigma_g^+ - X^3 \Sigma_g^-$ transition of the oxygen band system. Opt Spectrosc 1979;47(2):151–3.

[79] Gamache RR, Goldman A, Rothman LS. Improved spectral parameters for the three most abundant isotopomers of the oxygen molecule. J Quant Spectrosc Radiat Transfer 1998;59(3–5):495–509. http://dx.doi.org/10.1016/S0022-4073(97)00124-6.

[80] Robichaud DJ, Hodges JT, Brown LR, Lisak D, Masłowski P, Yeung LY, Okumura M, Miller CE. Experimental intensity and lineshape parameters of the oxygen A-band using frequency-stabilized cavity ring-down spectroscopy. J Mol Spectrosc 2008;248(1):1–13. http://dx.doi.org/10.1016/j.jms.2007.10.010.

[81] Havey DK, Long DA, Okumura M, Miller CE, Hodges JT. Ultra-sensitive optical measurements of high-J transitions in the O_2 A-band. Chem Phys Lett 2009;483(1–3):49–54. http://dx.doi.org/10.1016/j.cplett.2009.10.067.

[82] Drouin BJ, Benner DC, Brown LR, Cich MJ, Crawford TJ, Devi VM, Guillaume A, Hodges JT, Mlawer EJ, Robichaud DJ, et al. Multispectrum analysis of the oxygen A-band. J Quant Spectrosc Radiat Transfer 2017;186:118–38. http://dx.doi.org/10.1016/j.jqsrt.2016.03.037.

[83] Reed ZD, Tran H, Ngo HN, Hartmann J-M, Hodges JT. Effect of non-markovian collisions on measured integrated line shapes of CO. Phys Rev Lett 2023;130(14):143001. http://dx.doi.org/10.1103/PhysRevLett.130.143001.

[84] Tran H, Li G, Ngo NH, Ebert V. Non-impact effects in the absorption spectra of HCl diluted in CO_2, air, and He: Measurements and predictions. J Chem Phys 2023;158(18). http://dx.doi.org/10.1063/5.0147916.

[85] Tran H, Li G, Ngo NH, Ebert V. Pressure dependence of the measured line intensity and super-Lorentzian effects in the absorption spectra of pure HCl. Phys Chem Chem Phys 2023;25(15):10343–52. http://dx.doi.org/10.1039/D2CP04892B.

[86] Fleisher AJ, Adkins EM, Reed ZD, Yi H, Long DA, Fleurbaey HM, Hodges JT. Twenty-five-fold reduction in measurement uncertainty for a molecular line intensity. Phys Rev Lett 2019;123(4):043001. http://dx.doi.org/10.1103/PhysRevLett.123.043001.

[87] Predoi-Cross A, Hambrook K, Keller R, Povey C, Schofield I, Hurtmans D, Over H, Mellau GC. Spectroscopic lineshape study of the self-perturbed oxygen A-band. J Mol Spectrosc 2008;248(2):85–110. http://dx.doi.org/10.1016/j.jms.2007.11.007.

[88] Roland S, Learner RCM. Precise line parameters and transition probability of the atmospheric a band of molecular oxygen $^{16}O_2$. J Quant Spectrosc Radiat Transfer 1999;61(6):781–94. http://dx.doi.org/10.1016/S0022-4073(98)00066-1.

[89] Herman R, Wallis RF. Influence of vibration-rotation interaction on line intensities in vibration-rotation bands of diatomic molecules. J Chem Phys 1955;23(4):637–46. http://dx.doi.org/10.1063/1.1742069.

[90] Domysławska J, Wójtewicz S, Masłowski P, Cygan A, Bielska K, Trawiński RS, Ciuryło R, Lisak D. A new approach to spectral line shapes of the weak oxygen transitions for atmospheric applications. J Quant Spectrosc Radiat Transfer 2016;169:111–21. http://dx.doi.org/10.1016/j.jqsrt.2015.10.019.

[91] Domysławska J, Wójtewicz S, Masłowski P, Cygan A, Bielska K, Trawiński RS, Ciuryło R, Lisak D. Spectral line shapes and frequencies of the molecular oxygen B-band R-branch transitions. J Quant Spectrosc Radiat Transfer 2015;155:22–31. http://dx.doi.org/10.1016/j.jqsrt.2014.12.015.

[92] Wójtewicz S, Cygan A, Masłowski P, Domysławska J, Lisak D, Trawiński RS, Ciuryło R. Spectral line shapes of self-broadened P-branch transitions of oxygen B band. J Quant Spectrosc Radiat Transfer 2014;144:36–48. http://dx.doi.org/10.1016/j.jqsrt.2014.03.029.

[93] Gordon IE, Rothman LS, Toon GC. Revision of spectral parameters for the B- and γ-bands of oxygen and their validation against atmospheric spectra. J Quant Spectrosc Radiat Transfer 2011;112:2310–22. http://dx.doi.org/10.1016/j.jqsrt.2011.05.007.

[94] Domysławska J, Wójtewicz S, Masłowski P, Bielska K, Cygan A, Słowiński M, Trawiński RS, Ciuryło R, Lisak D. Line-shape analysis for high J R-branch transitions of the oxygen B band. J Quant Spectrosc Radiat Transfer 2020;242:106789. http://dx.doi.org/10.1016/j.jqsrt.2019.106789.

[95] Ciuryło R, Pine AS. Speed-dependent line mixing profiles. J Quant Spectrosc Radiat Transfer 2000;67(5):375–93. http://dx.doi.org/10.1016/S0022-4073(00)00030-3.

[96] Pine AS, Gabard T. Speed-dependent broadening and line mixing in CH_4 perturbed by Ar and N_2 from multispectrum fits. J Quant Spectrosc Radiat Transfer 2000;66(1):69–92. http://dx.doi.org/10.1016/S0022-4073(99)00222-8.

[97] Domysławska J, Wójtewicz S, Bielska K, Bilicki S, Ciuryło R, Lisak D. Line mixing in the oxygen B band head. J Chem Phys 2022;156:084301. http://dx.doi.org/10.1063/5.0079158.

[98] Bielska K, Domysławska J, Wójtewicz S, Balashov A, Słowiński M, Piwiński M, Cygan A, Ciuryło R, Lisak D. Simultaneous observation of speed dependence and Dicke narrowing for self-perturbed P-branch lines of O_2 B band. J Quant Spectrosc Radiat Transfer 2021;276:107927. http://dx.doi.org/10.1016/j.jqsrt.2021.107927.

[99] Bielska K, Tran DD, Balashov AA, Domysławska J, Wójtewicz S, Bober M, Bilicki S, Ciuryło R, Lisak D. Pressure and temperature dependencies of air-perturbed O_2 B-band line shapes. Spectrochim Acta Part A: Mol Biomol Spectrosc 2023;303:123185. http://dx.doi.org/10.1016/j.saa.2023.123185.

[100] Joint Committee for Guides in Metrology. Evaluation of measurement data—Guide to the expression of uncertainty in measurement. vol. 50, Geneva: Int. Organ. Stand.; 2008, p. 134. http://dx.doi.org/10.59161/jcgm100-2008e.

[101] Yang Z, Wennberg PO, Cageao RP, Pongetti TJ, Toon GC, Sander SP. Ground-based photon path measurements from solar absorption spectra of the O_2 A-band. J Quant Spectrosc Radiat Transfer 2005;90(3–4):309–21. http://dx.doi.org/10.1016/j.jqsrt.2004.03.020.

[102] Lewis BR, Gibson ST, Torop LW, McCoy DG. Quantum interference in the schumann-runge bands of the molecular oxygen. Geophys Res Lett 1998;25:2457–60. http://dx.doi.org/10.1029/98GL51783.

[103] Lewis BR, Gibson ST, Hawes FT, Torop LW. A new model for the Schumann–Runge bands of O_2. J Quant Spectrosc Radiat Transfer 2001;26:519–26. http://dx.doi.org/10.1016/S1464-1917(01)00040-X.

[104] Minschwaner K, Anderson GP, Hall LA, Yoshino K. Polynomial coefficients for calculating O_2 Schumann–Runge cross sections at 0.5 cm^{-1} resolution. Geophys Res: Atmos 1992;97:10103–8. http://dx.doi.org/10.1029/92JD00661.

[105] Yoshino K, Freeman DE, Esmond JR, Parkinson WH. High resolution absorption cross-sections and band oscillator strengths of the Schumann–Runge bands of oxygen at 79 K. Planet Space Sci 1987;35(8):1067–75. http://dx.doi.org/10.1016/0032-0633(87)90011-0.

[106] Veseth L, Lofthus A. Fine structure and centrifugal distortion in the electronic and microwave spectra of O_2 and SO. Mol Phys 1974;27(2):511–9. http://dx.doi.org/10.1080/00268977400100461.

[107] Lewis BR, Berzins L, Carver JH, Gibson ST. Rotational variation of predissociation linewidth in the Schumann–Runge bands of $^{16}O_2$. J Quant Spectrosc Radiat Transfer 1986;36:187–207. http://dx.doi.org/10.1016/0022-4073(86)90068-3.

[108] Lewis BR, Berzins L, Carver JH. Oscillator strengths for the Schumann–Runge bands of $^{16}O_2$. J Quant Spectrosc Radiat Transfer 1986;36(3):209–32. http://dx.doi.org/10.1016/0022-4073(86)90069-5.

[109] Tatum JB, Watson JKG. Rotational line strengths in $3\Sigma\pm$–$3\Sigma\pm$transitions with intermediate coupling. Can J Phys 1971;49(21):2693–703. http://dx.doi.org/10.1139/p71-32.

[110] Cheung ASC, Yoshino K, Esmond JR, Chiu SSL, Freeman DE, Parkinson WH. Predissociation linewidths of the (1,0)–(12,0) Schumann–Runge absorption bands of O2 in the wavelength region 179–202 nm. J Chem Phys 1990;92:842–9. http://dx.doi.org/10.1063/1.458117.

[111] Cheung AS-C, Yoshino K, Parkinson WH, Freeman DE. Molecular spectroscopic constants of O_2 ($B^3\Sigma_u^-$): The upper state of the Schumann–Runge bands. J Mol Spectrosc 1986;119(1):1–10. http://dx.doi.org/10.1016/0022-2852(86)90196-7.

[112] Ji A, Tomazzeli OG, Palancar GG, Chaverot G, Barker M, Fernández RP, Minschwaner K, Kasting JF. A correlated-k parameterization for O_2 photolysis in the Schumann–Runge bands” JGR: Atmospheres. JGR Atmos 2024;129:e2023JD040610. http://dx.doi.org/10.1029/2023JD040610.

[113] Tomazzeli OG, Palancar GG, Minchswaner K, Ji A, Madronich S, Fernandez RP. Impact of the overlapping O_2 Schumann–Runge and Herzberg continua with Schumann-Runge bands on photolysis rate coefficients: comparing the Koppers and Murtagh parameterization with line-by-line cross section. Journal of Quantitative Spectroscopy and Radiative Transfer 2025;109678. http://dx.doi.org/10.1016/j.jqsrt.2025.109678.

[114] Tan Y, Skinner FM, Samuels S, Hargreaves RJ, Hashemi R, Gordon IE. H_2, He, and CO_2 pressure-induced parameters for the HITRAN database. II. Line lists of CO_2, N_2O, CO, SO_2, OH, OCS, H_2CO, HCN, PH_3, H_2S, and GeH_4. Astrophys J Suppl Ser 2022;262(2):40. http://dx.doi.org/10.3847/1538-4365/ac83a6.

[115] Tan Y, Kochanov RV, Rothman LS, Gordon IE. Introduction of water-vapor broadening coefficients and their temperature dependence exponents into the HITRAN database, Part I: CO_2, N_2O, CO, CH_4, O_2, NH_3, and H_2S. 2019, http://dx.doi.org/10.1029/2019JD030929.

[116] Petrova TM, Solodov AM, Solodov AA, Deichuli VM, Fedorova AA. CO_2-broadened lineshapes in the oxygen A-band. J Quant Spectrosc Radiat Transfer 2024;314:108850. http://dx.doi.org/10.1016/j.jqsrt.2023.108850.

[117] Golubiatnikov GY, Koshelev MA, Krupnov AF. Reinvestigation of pressure broadening parameters at 60-GHz band and single 118.75GHz oxygen lines at room temperature. J Mol Spectrosc 2003;222(2):191–7. http://dx.doi.org/10.1016/j.jms.2003.08.002.

[118] Terragni J, Gordon IE, Adkins EM, Boulet C, Campargue A, Chistikov D, Finenko A, Finkenzeller H, Fleurbaey H, Hargreaves RJ, Hanson RK, Hartmann J-M, Klingberg A, Kohler E, Koroleva AO, Mondelain D, Piccioni G, Stefani S, Strand CL, Tran H, Turbet M, Vigasin A, Vitali F, Volkamer R, Wei C. Collision induced absorption in HITRAN2024: Enhanced and improved data for atmospheric and planetary studies. J Quant Spectrosc Radiat Transfer 2025. accepted.

[119] Stevenson LE, Laughner JL, Okumura M, Hodges JT, Adkins EM. Contributions of argon, nitrogen, and oxygen to air broadening in the oxygen A-band. J Quant Spectrosc Radiat Transfer 2025;342:109480. http://dx.doi.org/10.1016/j.jqsrt.2025.109480.

[120] Wulfmeyer V, Hardesty RM, Turner DD, Behrendt A, Cadeddu MP, Di Girolamo P, Schlüssel P, Van Baelen J, Zus F. A review of the remote sensing of lower tropospheric thermodynamic profiles and its indispensable role for the understanding and the simulation of water and energy cycles. Rev Geophys 2015;53(3):819–95. http://dx.doi.org/10.1002/2014RG000476.

[121] Gallucci D, Cimini D, Turner E, Fox S, Rosenkranz PW, Tretyakov MY, Mattioli V, Larosa S, Romano F. Uncertainty in simulated brightness temperature due to sensitivity to atmospheric gas spectroscopic parameters from the centimeter-to submillimeter-wave range. Atmos Chem Phys 2024;24:7283–308. http://dx.doi.org/10.5194/ACP-24-7283-2024.

[122] Makarov DS, Tretyakov MY, Rosenkranz PW. 60-GHz oxygen band: Precise experimental profiles and extended absorption modeling in a wide temperature range. J Quant Spectrosc Radiat Transfer 2011;112:1420–8. http://dx.doi.org/10.1016/j.jqsrt.2011.02.018.

[123] Makarov DS, Tretyakov MY, Boulet C. Line mixing in the 60-GHz atmospheric oxygen band: Comparison of the MPM and ECS model. J Quant Spectrosc Radiat Transfer 2013;124:1–10. http://dx.doi.org/10.1016/j.jqsrt.2013.02.019.

[124] Koshelev MA, Vilkov IN, Tretyakov MY. Collisional broadening of oxygen fine structure lines: The impact of temperature. J Quant Spectrosc Radiat Transfer 2016;169:91–5. http://dx.doi.org/10.1016/j.jqsrt.2015.09.018.

[125] Makarov DS, Tretyakov MY, Rosenkranz PW. Revision of the 60-GHz atmospheric oxygen absorption band models for practical use. J Quant Spectrosc Radiat Transfer 2020;243:106798. http://dx.doi.org/10.1016/j.jqsrt.2019.106798.

[126] Koshelev MA, Vilkov IN, Makarov DS, Tretyakov MY, Rosenkranz PW. Speed-dependent broadening of the O 2 fine-structure lines. J Quant Spectrosc Radiat Transfer 2021;264:107546. http://dx.doi.org/10.1016/j.jqsrt.2021.107546.

[127] Koshelev MA, Vilkov IN, Galanina TA, Serov EA, Makarov DS, Tretyakov MY. Temperature behavior of collisional parameters of oxygen fine-structure lines: O2-O2 case. J Quant Spectrosc Radiat Transfer 2023;298:108493. http://dx.doi.org/10.1016/j.jqsrt.2023.108493.

[128] Tran DD, Sironneau VT, Hodges JT, Armante R, Cuesta J, Tran D. Prediction of high-order line-shape parameters for air-broadened O_2 lines using requantized classical molecular dynamics simulations and comparison with measurements. J Quant Spectrosc Radiat Transfer 2019;222–223:108–14. http://dx.doi.org/10.1016/j.jqsrt.2018.10.013.

[129] Gancewski M, Jóźwiak H, Quintas-Sánchez E, Dawes R, Thibault F, Wcisło P. Fully quantum calculations of O_2–N_2 scattering using a new potential energy surface: Collisional perturbations of the oxygen 118 GHz fine structure line. J Chem Phys 2021;155:124307. http://dx.doi.org/10.1063/5.0063006.

[130] Wcisło P, Thibault F, Stolarczyk N, Jóźwiak H, Słowiński M, Gancewski M, Stankiewicz K, Konefał M, Kassi S, Campargue A, Tan Y, Wang J, Patkowski K, Ciuryło R, Lisak D, Kochanov R, Rothman LS, Gordon IE. The first comprehensive dataset of beyond-voigt line-shape parameters from *ab initio* calculations for the HITRAN database: He-perturbed H_2 case study. J Quant Spectrosc Radiat Transfer 2021;260:107477. http://dx.doi.org/10.1016/j.jqsrt.2020.107477.

[131] Stankiewicz K, Stolarczyk N, Jóźwiak H, Thibault F, Wcisło P. Accurate calculations of beyond-voigt line-shape parameters from first principles for the he-perturbed HD rovibrational lines: A comprehensive dataset in the HITRAN DPL format. J Quant Spectrosc Radiat Transfer 2021;276:107911. http://dx.doi.org/10.1016/j.jqsrt.2021.107911.

[132] Słowiński M, Thibault F, Tan Y, Wang J, Liu A-W, Hu S-M, Kassi S, Campargue A, Konefał M, Jóźwiak H, Patkowski K, Żuchowski P, Ciuryło R, Lisak D, Wcisło P. H_2-He collisions *Ab initio* theory meets cavity-enhanced spectra. Phys Rev A 2020;101:052705. http://dx.doi.org/10.1103/PhysRevA.101.052705.

[133] Stankiewicz K, Jóźwiak H, Gancewski M, Stolarczyk N, Thibault F, Wcisło P. *Ab initio* calculations of collisional line–shape parameters and generalized spectroscopic cross-sections for rovibrational dipole lines in HD perturbed by He. J Quant Spectrosc Radiat Transfer 2020;254:107194. http://dx.doi.org/10.1016/j.jqsrt.2020.107194.

[134] Lamperti M, Rutkowski L, Ronchetti D, Gatti D, Gotti R, Cerullo G, Thibault F, Jóźwiak H, Wójtewicz S, Masłowski P, Wcisło P, Polli D, Marangoni M. Stimulated Raman scattering metrology of molecular hydrogen. Commun Phys 2023;6:67. http://dx.doi.org/10.1038/s42005-023-01187-z.

[135] Jóźwiak H, Stolarczyk N, Stankiewicz K, Zaborowski M, Lisak D, Wójtewicz S, Jankowski P, Patkowski K, Szalewicz K, Thibault F, Gordon IE, Wcisło P. Accurate reference spectra of HD in an H_2-He bath for planetary applications. Astron Astrophys 2024;687:A69. http://dx.doi.org/10.1051/0004-6361/202449889.

[136] Cygan A, Wójtewicz S, Jóźwiak H, Kowzan G, Stolarczyk N, Bielska K, Wcisło P, Ciuryło R, Lisak D. Dispersive heterodyne cavity ring-down spectroscopy exploiting eigenmode frequencies for high-fidelity measurements. Sci Adv 2025;11:eadp8556. http://dx.doi.org/10.1126/sciadv.adp8556.

[137] Olejnik A, Jóźwiak H, Gancewski M, Quintas-Sánchez E, Dawes R, Wcisło P. *Ab initio* quantum scattering calculations and a new potential energy surface for the $HCl(X^1\Sigma^+)$–$O_2(X^3\Sigma_g^-)$ system: Collision-induced line shape parameters for O_2-perturbed R(0) 0–0 line in $H^{35}Cl$. J Chem Phys 2023;159:134301. http://dx.doi.org/10.1063/5.0169968.

[138] Tran H, Li G, Ebert V, Hartmann J-M. Super-and sub-Lorentzian effects in the Ar-broadened line wings of HCl gas. J Chem Phys 2017;146(19). http://dx.doi.org/10.1063/1.4983397.

[139] Birk M, Röske C, Wagner G. The pressure dependence of the experimentally-determined line intensity and continuum absorption of pure CO_2 in the 1.6 μm region. J Quant Spectrosc Radiat Transfer 2024;324:109055. http://dx.doi.org/10.1016/j.jqsrt.2024.109055.

[140] Camy-Peyret C, Vigasin AA. Weakly interacting molecular pairs: Unconventional absorbers of radiation in the atmosphere. vol. 27, Springer Science & Business Media; 2003.

[141] Maté B, Lugez C, Fraser GT, Lafferty WJ. Absolute intensities for the O_2 1.27 μm continuum absorption. J Geophys Res: Atmos 1999;104(D23):30585–90. http://dx.doi.org/10.1029/1999JD900824.

[142] Tran H, Boulet C, Hartmann J-M. Line mixing and collision-induced absorption by oxygen in the a band: Laboratory measurements, model, and tools for atmospheric spectra computations. J Geophys Res: Atmos 2006;111(D15). http://dx.doi.org/10.1029/2005JD006869.

[143] Spiering FR, Kiseleva MB, Filippov NN, Naus H, van Lieshout B, Weijenborg C, van der Zande WJ. Line mixing and collision induced absorption in the oxygen A-band using cavity ring-down spectroscopy. J Chem Phys 2010;133(11). http://dx.doi.org/10.1063/1.3460924.

[144] Long DA, Robichaud DJ, Hodges JT. Frequency-stabilized cavity ring-down spectroscopy measurements of line mixing and collision-induced absorption in the O_2 A-band. J Chem Phys 2012;137(1):014307. http://dx.doi.org/10.1063/1.4731290.

[145] Kassi S, Guessoum S, Abanto JA, Tran H, Campargue A, Mondelain D. Temperature dependence of the collision-induced absorption band of O_2 near 1.27 μm. J Geophys Res: Atmos 2021;126(13):e2021JD034860. http://dx.doi.org/10.1029/2021JD034860.

[146] Karman T, Koenis MA, Banerjee A, Parker DH, Gordon IE, van der Avoird A, van der Zande WJ, Groenenboom GC. O_2- O_2 and O_2- N_2 collision-induced absorption mechanisms unravelled. Nat Chem 2018;10(5):549–54. http://dx.doi.org/10.1038/s41557-018-0015-x.

[147] Adkins EM, Karman T, Campargue A, Mondelain D, Hodges JT. Parameterized model to approximate theoretical collision-induced absorption band shapes for O_2-O_2 and O_2-N_2. J Quant Spectrosc Radiat Transfer 2023;310:108732. http://dx.doi.org/10.1016/j.jqsrt.2023.108732.

[148] Serov EA, Stolarczyk N, Makarov DS, Vilkov IN, Golubiatnikov GY, Balashov AA, Koshelev MA, Wcisło P, Thibault F, Tretyakov MY. CO-Ar collisions: ab initio model matches experimental spectra at a sub percent level over a wide pressure range. J Quant Spectrosc Radiat Transfer 2021;272:107807. http://dx.doi.org/10.1016/j.jqsrt.2021.107807.